Faculty of Physics and Astronomy

University of Heidelberg

Diploma Thesis
in Physics

written by

Michael Schneider
born in Mannheim

July 2001

Studies for neutron tomography at the Institute Laue-Langevin

This diploma thesis was written by
Michael Schneider
at the
INSTITUTE OF PHYSICS
HEIDELBERG
Supervisor:
Priv. Doz. Dr. Hartmut Abele.

Abstract

Studies for neutron tomography at the Institute Laue-Langevin

Neutron computer tomography allows the reconstruction of the three dimensional structure of an object from a set of projections. The 58MW high flux reactor of the Institute Laue-Langevin provides a thermal neutron beam with a flux of $2.9 \times 10^9 n/cm^2 s$ for the installation of a tomography facility. The aim of this tomography facility will be to visualize dynamic processes and to implement very fast reconstruction methods. A first step in this direction was the installation of a temporary tomography setup. Already with this setup at a well collimated cold neutron beam, the neutron flux was higher than at any other existing tomography station. This thesis describes the measurement of the beam properties for the final tomography station as well as the preparative measurements with the temporary tomography setup. These experiments provide useful experience, which will be used for the installation of the final facility.

Untersuchungen zur Neutronentomographie am Institut Laue-Langevin

Neutronen-Computertomographie ermoeglicht die Rekonstruktion der dreidimensionalen Struktur eines Objekts aus einer Serie von Projektionsaufnahmen. Am 58MW Hochflussreaktor des Instituts Laue-Langevin steht ein Strahl thermischer Neutronen mit einem Flu von $2.9 \times 10^9 n/cm^2 s$ fuer die Einrichtung einer Tomographieanlage zur Verfuegung. Das Ziel dieser Anlage wird die Visualisierung dynamischer Prozesse und die Implementierung sehr schneller Rekonstruktionsverfahren sein. Ein erster Schritt in diese Richtung war die Installation eines temporaeren Tomographieexperiments. Schon mit dieser Anlage an einem gut kollimierten Strahl von kalten Neutronen war der Neutronenfluss hoeher als an jeder anderen existierenden Tomographieanlage. Diese Diplomarbeit beschreibt zum einen die Messung der Strahleigenschaften fuer die endgueltige Tomographiestation und zum anderen die vorbereitenden Messungen an der temporaeren Tomographiestation. Diese Experimente lieferten nuetzliche Erfahrungen, die bei der Einrichtung der endgueltigen Tomographiestation genutzt werden.

Contents

Chapter 1

Overview

1.1 Motivation for neutron tomography

Computer tomography allows the reconstruction of the three dimensional structure of an object from a set of projection images. A projection image is a radiograph of an object taken at a certain angle.

In recent years, impressive pictures of neutron radiography and neutron tomography applications have been published by facilities like the Technische Universitaet Muenchen (see [Sch99]), the Paul Scherrer Institute in Villingen (CH)(see [Leh99]) and many others. Some of the reported radiography applications use exposure times of several hours. This indicates that tomography needs a high neutron flux from a reactor or spallation source. A list of references to 11 neutron tomography facilities worldwide can be found in Chapter I.1 of [Sch99].

Figure 1.1 shows the reconstruction of a spark plug from a set of 180 neutron radiographs, each taken with an exposure time of 20s. The measurements were done at the Pf1b cold neutron beam of the Institute Laue-Langevin (ILL) in Grenoble. The 3D model of the reconstructed data shows the inside structure of the spark plug with a resolution of about 0.4mm, demonstrating the power of neutron tomography for non destructive testing of industrial parts at the ILL.

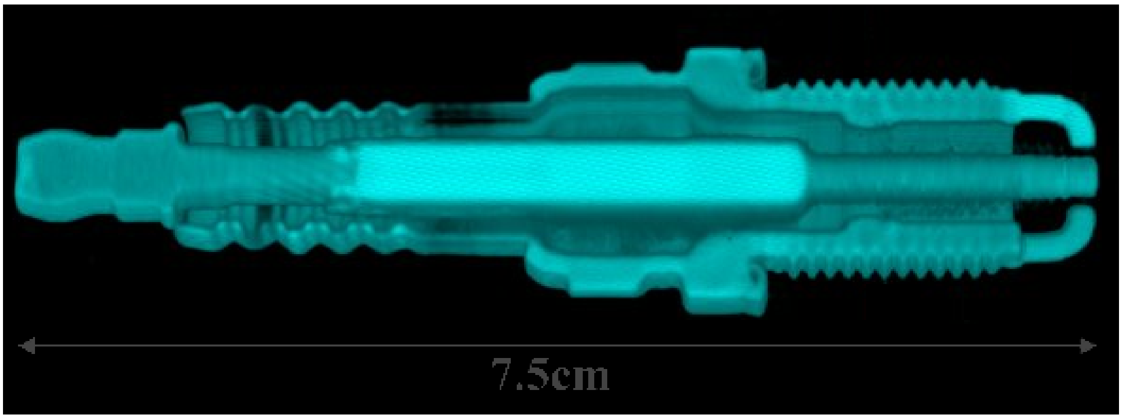

Figure 1.1: Neutron tomography of a spark plug at the Pf1b cold neutron beam of the Institute Laue-Langevin

So far, the availability of intense neutron beams is limited for technical reasons. However, at the high flux neutron source of the Institute Laue-Langevin, a thermal neutron beam with $2.9 * 10^9 \frac{n}{cm^2 s}$ is available for the installation of a tomography facility. The scope of the the neutron tomography facility at the ILL is the visualization of dynamic processes and the implementation of rapid reconstruction methods. Using the high flux in combination with an effective

detector system, exposure times down to 1ms for a single projection become possible. The performance of today's computer hardware allows a fast implementation of the reconstruction process. The reconstruction algorithm can be performed very rapidly if it is optimized to run on a multiprocessor computer architecture. The image acquisition and reconstruction system can be completely automated so that reconstruction of the data can be performed online.
In consideration of these preconditions, here is a list of possible applications for the ILL's tomography facility:

- Radiography:
    - Density profiling of gases in ultra-centrifuges
    - Observation of gas bubbles in heat exchangers under overload
- Tomography:
    - Cracks or Welding defects in metal parts
    - Chemical composition gradients
    - Sub resolution detection of cavities by diffusion of Gd
- Fast tomography:
    - Cyclic processes: Motor oil or fuel distribution during the combustion process
    - Diffusion processes
    - Density profiling of steam pressure in turbines under working conditions

Rather than to compete with existing projects on the improvement of spatial resolution of object details, the aim of the ILLs tomography project is to explore the possibilities that arise from the high flux reactor. On the cost of spatial resolution, the setup is optimized for a break off to new frontiers in the time domain.

1.2 Neutron tomography in comparison with other tomography methods

Computer tomographic reconstruction is based on a mathematical framework developed by Johann Radon back in 1917. It can be performed with projections produced by any kind of radiation capable of penetrating the sample. Which type of radiation is suited best for a certain purpose depends on the properties of the sample materials. The reconstruction process, however, doesn't depend on the kind of radiation used for taking the projections.
Tomography is well known today for its medical applications. Computer tomography with X-rays has been a diagnostic standard for many years. There is a wide range of applications based on the reconstruction of a sample from projections like electron tomography of biological objects with an electron microscope or non-destructive testing of industrial products and materials.
But there are also other types of tomography. Nuclear magnetic resonance tomography is a technique, that doesn't use projection images at all. The idea is to fulfill the condition for a measurable resonance signal at only one single point within the object at a time. The measurement is repeated for every point of the sample according to the resolution of the setup and immediately yields the desired value at this point. Once the volume is scanned completely, there is no need for further reconstruction. Positron emission tomography (PET) reconstructs the distribution of a radioactive substance brought into the volume of interest (for example a patients head) by tracking the products of the nuclear decay after they have left the volume.
Computer tomography is performed with various kinds of radiation. The interaction of X-rays with matter depends heavily on the atomic number. It increases with Z^4 because it is due to

electromagnetic interaction with the charge distribution of the atomic structure of matter. Usually X-ray tomographs work with a cone beam geometry due to the creation of the X-rays on a cathode, which can be regarded as a point like source.

Gamma-rays are photons with much higher energies than X-rays. Their ability to penetrate matter is higher because the interaction probability decreases for higher energies. However, the damage produced by gamma rays is higher, because the energy deposition in the sample increases with the energy of the photons.

Tomography with an electron microscope uses a parallel beam. The energy deposition in the sample is high. The samples are often frozen - cryo samples - and the number of exposures per sample is limited to a few angles.

Neutrons interact with the nuclei of the penetrated matter by the strong interaction, and the cross section doesn't show such uniform dependency on Z. In fact, neighboring elements in the periodic system and even isotopes of the same element can show quite different strengths of interaction with neutrons. In special cases the electromagnetic interaction of the neutrons magnetic moment with the sample could also become important for radiography.

In comparison to other radiation types neutrons special properties concerning tomography applications are:

- Penetrate all metals
- Light atoms can be seen
- Little energy deposition
- Parallel beam geometry

Chapter 2

Physical and technical background

2.1 Interaction between a neutron beam and matter

As an uncharged particle, the neutron doesn't interact with the electrostatic potential of protons and electrons within matter. It can interact with matter through its magnetic moment or by strong interaction. Here we consider two processes that lead to attenuation of the beam. These are scattering and absorption due to strong interaction. Scattering can furthermore be coherent and incoherent. In most cases the coherent part of the scattering cross section can be ignored in neutron tomography applications. In contrast to electromagnetic interaction (X-rays, e^-), the neutron cross sections are not correlated to the atomic number of the elements by a simple law. In fact, they can differ notably between two isotopes of the same element.

In contrary to the scattering cross section, the absorption cross section depends on the neutron energy. The absorbtion cross sections listed in table 2.1 hold for neutrons with velocity v=2200m/s (thermal neutrons). For the absorption of a neutron with velocity v_n these values need to be corrected by a factor v_n^{-1}. The formula for the total cross section for neutrons with velocity v_n becomes

$$\sigma = \sigma_s + \frac{2200\frac{m}{s}}{v_n}\sigma_{a,2200} \tag{2.1}$$

In a simple model the incoming neutron beam intensity is reduced through loss of neutrons that are absorbed or scattered, making the assumption that none of the scattered neutrons will hit the detector area.

$$\frac{I}{I_0} = \exp\Big(-\alpha x\Big) = \exp\Big(-\sigma\rho\frac{N_A}{M_{Mol}}x\Big) \tag{2.2}$$

I/I_0 = Relative beam intensity
α = Attenuation coefficient
σ = Total cross section
ρ = Density of the attenuating isotope
N_A = Avogadro Number
M_{Mol} = Molar mass of the target

Table 2.1 shows incoherent scattering and absorption cross sections of several materials. The wide differences between the cross sections are visible here. Because of its very high absorption cross section, ^{10}B is commonly used as neutron absorber for shielding against neutrons and in beam stops. Note the big difference in the cross sections of the boron isotopes. The three metals in table 2.1 can be considered typical sample materials. They show moderate attenuation. The density of hydrogen was assumed according to its concentration in water. Its concentration in plastic and organic substances is quite similar. The attenuation by the other elements in these materials is much lower, and so the values in the first line serve as an estimation for the attenuation by

			Attenuation I/I_0					
	σ_{s_i}	$\sigma_{a,2200}$	thermal beam ($v_n = 2200m/s$)			cold beam ($v_n = 700m/s$)		
			d=1mm	d=1cm	d=10cm	d=1mm	d=1cm	d=10cm
^1H	80.3	0.333	0.838	0.170	10^{-8}	0.606	6.7×10^{-3}	10^{-22}
^{10}B	3.0	3835	10^{-7}	10^{-66}	10^{-660}	10^{-19}	10^{-186}	10^{-1859}
^{11}B	0.21	0.0055	0.998	0.992	0.922	0.999	0.991	0.918
^{27}Al	0.008	0.231	0.999	0.986	0.866	0.996	0.961	0.672
^{56}Fe	0	2.59	0.978	0.803	0.112	0.940	0.539	2.1×10^{-3}
^{63}Cu	0.006	4.50	0.962	0.680	0.021	0.897	0.337	10^{-5}

Table 2.1: Incoherent scattering and absorption cross sections of some materials and the resulting attenuation of cold and thermal neutron beams. The coherent part of the scattering cross section can be ignored in neutron tomography applications. For the calculation of the attenuation, the density of H was assumed according to its concentration in water. The density of the boron isotopes was assumed according to its concentration in B_4C plastic (used for shielding and in beam stops) with 100% ^{10}B and ^{11}B, respectively

these materials. The high scattering cross section of hydrogen gives water, plastic and organic substances a good contrast in neutron radiographic images.

Usually, a sample material consists of more than one element or at least of several isotopes. For a region in the sample with constant density of all isotopes, the equation for the attenuation becomes

$$\frac{I}{I_0} = \exp\Big(- \sum_i \alpha_i x \Big) = \exp\Big(- \sum_i \sigma_i \rho_i \frac{N_A}{M_{Mol,i}} x \Big) \tag{2.3}$$

For an arbitrary distribution 2.3 can be written in the general form

$$\frac{I}{I_0} = \exp\Big(- \int_S \alpha(\vec{x}) ds \Big) \tag{2.4}$$

integrating along a straight line S, with the attenuation coefficient

$$\alpha(\vec{x}) = \sum_i \alpha_i(\vec{x}) = \sum_i \frac{\sigma_i \rho_i(\vec{x})}{M_{Mol,i}} N_A \tag{2.5}$$

Since the absorption cross section depends on v_n^{-1}, slower neutrons are attenuated stronger than faster ones. This fact is also reflected in table 2.1. For a neutron beam with given energy spectrum this means that the spectrum of the attenuated beam is shifted to higher energies.

Tests with aluminium indicated, that the effects of small angle scattering should be negligible. 20mm of aluminum put in the beam behind two hole apertures of diameter 2mm and 1mm with distance of 1.5m produced no macroscopically visible scattering patterns on a detector placed in 1.2m distance from the aluminum.

The effects of the neutrons magnetic moment are a valuable tool in solid state physics for the determination of material properties. However, they shall be neglected in this context, because for most sample materials they will be dominated by the effects of the strong interaction. For materials with distinct magnetic properties they have to be taken into account.

2.2 Reconstruction algorithm for tomography

2.2.1 The tomography principle

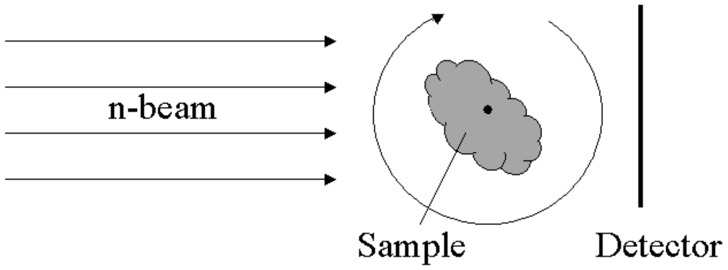

Figure 2.1: Tomography principle. The sample is rotated to take projection images at different angles.

Tomography is a method to retrieve the complete three dimensional structure of an object from a set of projections. Any kind of radiation capable of penetrating the sample can be used to produce the projections. The projections are obtained from radiographic images, that is grey value images resembling the intensity distribution of the used radiation after penetrating the sample. Since the properties of the beam are not of interest, the intensity is normalized to the beam intensity measured without any sample. Usually, the beam and the detector are fixed and the sample is rotated to take the projection images. The problem can be solved in two dimensions and carried out independently for different vertical slices of the object. The number of slices depends on the resolution of the detector. The theory used for the reconstruction is based on a work by Johann Radon back in 1917 (see [Rad17]). To use this theory for neutron tomography, it is necessary to make the following assumptions:

- The neutron beam is exactly parallel. With this assumption we can treat all vertical layers independently because their projections don't affect each other. If the beam direction changes over the beam cross section we will have to introduce corrections.

- The neutron beam is monoenergetic. Thus there are no effects from the energy dependence of the cross sections. The interaction with the sample is considered the same for all the neutrons in the beam and everywhere in the sample.

A detailed presentation of the tomographic reconstruction can be found in [Bil01]. The following description of the basic concepts is kept in the style and terminology used there.

2.2.2 Radon transformation

A projection λ of a function $f(\vec{r})$ of the two dimensional vector $\vec{r}$ is defined by the integral

$$\lambda_{\Phi}(p) = \int_A f(\vec{r})\delta(p - \vec{r} \cdot \vec{n}_{\Phi})d^2r \tag{2.6}$$

where Φ is the projection angle and p is the distance of the projection line from the coordinate origin (see figure 2.2).

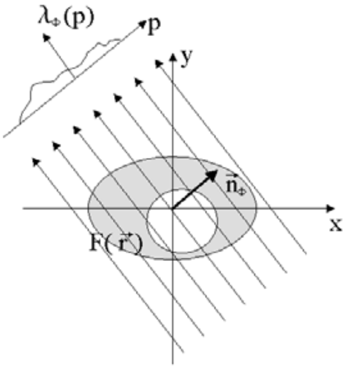

Figure 2.2: Projection in two dimensions

The δ-function in 2.6 resembles the fact that the projection takes place along a line in the 2 dimensional reconstruction volume. Comparison with equation 2.4 shows, that in tomography $f(\vec{r})$ corresponds to the attenuation coefficient. The negative natural logarithm of the normalized intensity -ln(I/I$_0$) measured in a pixel of the projection images corresponds to the projection 2.6 along one projection line. The problem of tomographic reconstruction now consists of finding the inverse of the Radon transformation.

2.2.3 Central slice theorem

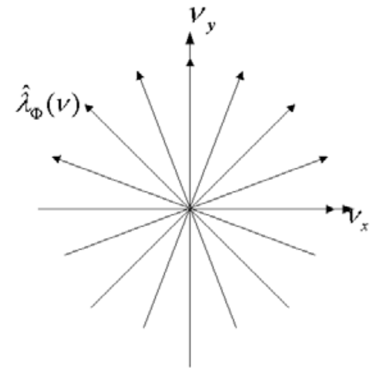

Figure 2.3: Projection data in fourier space according to the central slice theorem

The fourier transform $\hat{\lambda}_\Phi(\nu)$ of a projection $\lambda_\Phi(p)$ of the function $f(\vec{r})$ contains the values of the fourier transform $\hat{f}(\vec{\nu})$ along a line of angle Φ through the origin of the fourier space. This also holds in three dimensions and is therefore called the central slice theorem. As can be seen from figure 2.3, the reconstruction of $f(\vec{r})$ consists of an interpolation of $\hat{f}(\vec{\nu})$ from the central slices $\hat{\lambda}_\Phi(\nu)$. The interpolation, however, is difficult and not free of artifacts. Therefore, the standard method for reconstruction is the filtered back projection.

2.2.4 Filtered back projection

The filtered back projection avoids completely the fourier transform by performing all operations in real space.

A filter has to be applied to the projection data. This operation in real space corresponds to a weighting of the fourier transformed data shown in figure 2.3 by a factor $|\nu|$. This compensates the fact that the density of the indicated projection lines decreases as $1/|\nu|$. For a discrete implementation the most frequently used filters are the filters of Ramachandran and Lakshiminarayanan (RamLak or R&L filter)

$$h_r(n\Delta p) = \begin{cases} \frac{1}{4\Delta p^2} & for \quad n = 0 \\ 0 & for \quad \text{n even}, n \neq 0 \\ -\frac{1}{n^2\pi^2\Delta p^2} & for \quad \text{n odd} \end{cases} \tag{2.7}$$

and Shepp and Logan (ShepLoagan or S&L filter)

$$h_s(n\Delta p) = -\frac{2}{\pi^2\Delta p^2(4n^2-1)} \tag{2.8}$$

The filtered projection profiles $\lambda_\Phi(p)$ are then simply projected back to the reconstruction plane and summed over Φ. (figure 2.4).

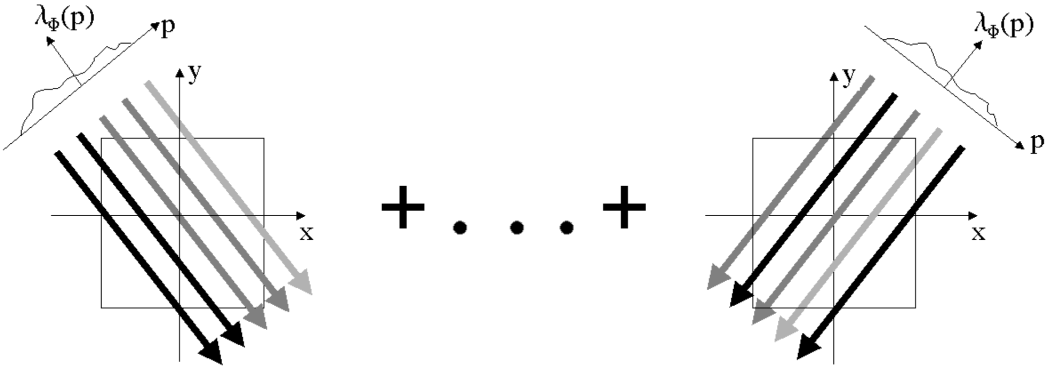

Figure 2.4: Backprojection. The filtered projection profiles are projected back to the reconstruction plane and summed over Φ.

The effect of the filters in real space can easily be understood from a simple example. If $f(\vec{r}) = \delta(\vec{r_0})$, then all the projections are also δ-functions. Back projection of all these δ-functions to the projection plane will give a pattern that looks similar to the one in figure 2.3 but in real space. The result of the combined operations Radon transformation and simple back projection of the δ-function without filter is $1/|\vec{r} - \vec{r_0}|$. Thus the mere projection and back projection corresponds to a convolution of the object with $1/|\vec{r}|$. The filters 2.7 and 2.8 are therefore inverse 1/r filters. A convolution in real space corresponds to a multiplication in fourier space. Therefore, the inverse of a filter can be easily determined by taking the reciprocal values of its fourier transform, which, however, can be very large or even infinite. The RamLak and ShepLoagan filters are discrete solutions for this problem, which must be seen as compromises between prevention of such large or infinite values and an ideal reconstruction.

2.2.5 The Nyquist condition

The Nyquist condition states that a function f(x) can be reconstructed from its values at positions $x = n\Delta p$, n=-N,...,N if $\Delta p \leq (2\nu_{max})^{-1}$, where ν_{max} is the maximum spatial frequency in the spectrum of f(x). The number of detection points per unit length must be greater than double the maximum frequency in the object. This is the condition for a simple 2d image.
For the number of angles needed for an artifact free reconstruction from projections we can find

a similar condition by considering the maximum frequency of the object. It defines a circle in the fourier space, outside of which all values of the projection slices are zero. At ν_{max} the distance between the slices $\nu\Delta\Phi$ is maximal. It must be less than $(2r_{max})^{-1}$ according to the Nyquist condition and we get the maximum angle between two projections

$$\Delta\Phi \leq \frac{1}{2r_{max}\nu_{max}} \tag{2.9}$$

and the required number of projections is

$$M \geq \frac{\pi}{\Delta\Phi_{max}} = 2\pi r_{max}\nu_{max} \tag{2.10}$$

2.3 General limitations for neutron radiographic images taken with a scintillator and CCD camera system

The most convenient detector system for neutron radiography and tomography is a combination of a scintillator and a CCD camera. For a discussion on the use of other types of detectors for this purpose see chapter I.3 of [Sch99].

2.3.1 Limiting factors

The focus of this section is on the quality of the projection images. The problems arising from the tomographic reconstruction will be discussed in chapter 3. For building a tomography setup various limitations are imposed by the different parts of the experiment. The components have to be carefully chosen to achieve a good result. The following table contains the properties of an experimental setup with a scintillator and CCD camera that determine the quality of the radiographic images. The different components have their specific crucial properties for the experiment. Their resulting effects on the image properties will be discussed below.

Neutron beam	Intensity Beam divergence Neutron statistics Spatial and temporal homogenity
Scintillator	Point spread function of the scintillator (see section 2.3.2) Quantum efficiency and light output per neutron Photon statistics
Optical system	Distance lens-scintillator Objective parameters Geometric aberrations
CCD chip	Chip and pixel size Dynamic range of the output signal Sensitivity of the CCD chip CCD camera noise

2.3.2 Spatial resolution

The spatial resolution of a radiography experiment describes how a sharp image is smeared out during the process of image acquisition. It indicates the amount of details contained in the sample that can be resolved by the system. We will discuss this by what is called the point spread function.

As described in [Jae97], the point spread function (PSF) of an imaging system defines the image the system produces of a point like object. The point spread function of an ideal imaging system would be a point or, mathematically spoken, a δ-function. We can consider an arbitrary image to be made up of a large number of point like objects. Once the point spread function is determined, we can determine the image the system produces of a known object. It is just the sum of the point spread functions of all the points in the object. We will see in this section, why it is impossible to reconstruct an image perfectly even though the point spread function is known precisely.

Considering the image that would be produced by an ideal imaging system, we can find a mathematical expression for the actual image: The Image g of an arbitrary object is the ideal image g_0 convolved with the point spread function h of the imaging system.

$$g = h * g_0 \tag{2.11}$$

$$g(x,y) = \int g_0(x',y')h(x-x',y-y')dx'dy' \tag{2.12}$$

It is useful to determine how certain frequencies are affected by the image acquisition process. Therefore, we look what happens in the fourier space. Here the convolution corresponds to a simple multiplication.

$$\hat{g}(\nu_x,\nu_y) = \hat{g}_0(\nu_x,\nu_y)\hat{h}(\nu_x,\nu_y) \tag{2.13}$$

A general imaging system has a maximum spatial frequency. All frequencies above this maximum frequency are not represented in the images taken by the system. In the discrete case the image is an array of pixels, and the maximum frequency is naturally limited by the number of pixels. In fourier space the existence of a maximum frequency is resembled by the fact that the fourier transform $\hat{h}$ of the point spread function is zero except within a region around the origin where $\nu < \nu_{max}$. This shows that it is impossible to reconstruct the ideal image g_0. The inverse filter

$$\hat{h}^{-1}(\nu_x,\nu_y) = \frac{1}{\hat{h}(\nu_x,\nu_y)} \tag{2.14}$$

has infinite values at least everywhere outside the region with $\nu < \nu_{max}$.

Now we are going to consider the point spread function of a scintillator camera system. There are three components determining the point spread function of the system: The beam divergence, the size and brightness of the spot produced by a single neutron on the scintillator and the PSF of the camera itself.

$$g = h_d * h_{sc} * h_{ca} * g_0 \tag{2.15}$$

The scintillator spot is in the μm range and therefore far beyond the limitations imposed by the beam divergence and camera resolution and will be considered a δ-function. Still, the intensity of the spot plays a role and will be represented by the constant factor a_{sc} which leaves

$$g = h_d * h_{ca} * a_{sc}g_0 \tag{2.16}$$

The point spread function of the camera resembles the process of sampling the continuous image to a discrete set of pixel values. The point spread function has the shape of a pixel. Its fourier transform is a function of type $\sin(a\nu)/\nu$. It has finite values after a null at $a\nu = \pi$. Thus there can be certain frequencies present in the image while other lower frequencies are completely suppressed. This is not desirable because the resulting information in the image is not reliable. In practice the resolution of the camera will be chosen so that the Nyquist condition discussed in section 2.2.5 holds for the given beam divergence. This avoids such effects.

The beam divergence is often given as L/D value or in rad. L is the distance of the view point from the source and D is the diameter of the source. The same relation holds for the size D' of the image of a point like object (PSF) to the distance L' between the detector and the object.

$$\frac{L}{D} = \frac{L'}{D'} \tag{2.17}$$

For example, for the measurements at the Pf1b beam position described in chapter 3 the L/D ratio was 333, which corresponds to a spatial resolution of 0.3mm for a detector distance of 10cm from the sample. If the divergence is given in rad, this indicates the angle under which D is seen from a distance L.

$$\phi[rad] = \arctan(D/L) \tag{2.18}$$

This is about D/L, since D<<L for any reasonable divergence values.

If there are abberations of the camera optic that lead to geometric distortions of the image, it is possible to correct for that by a geometric transformation. In general this requires interpolation of the pixel values which requires a lot of computing power. Thus aberration should be avoided if possible.

2.3.3 Grey value resolution

The range of gray values of a projection image taken with a digital camera is determined by the D/A converter of the CCD chip. A 12bit CCD chip has a dynamic range R_d of $2^{12} = 4096$. However, the effective dynamic range is limited by noise. To detect a difference in the gray value the difference in the count rate must be larger than the noise level. The effective dynamic range is R_d/R_n. With a noise rate of 4 counts per pixel RMS a 12bit chip can use a dynamic range of 1024. The error of the gray values is R_n. The error for the attenuation $\frac{I}{I_0}$ is obtained through the relative errors of I and I_0

$$\Delta\frac{I}{I_0} = \frac{I}{I_0}\sqrt{\left(\frac{R_n}{I}\right)^2 + \left(\frac{R_n}{I_0}\right)^2} = \frac{R_n}{I_0}\sqrt{1+\frac{I^2}{I_0^2}} \tag{2.19}$$

If I_0 is the maximum count rate R_d we get

$$\Delta\frac{I}{I_0} = \frac{R_n}{R_d}\sqrt{1+\frac{I^2}{R_d^2}} \tag{2.20}$$

What difference in attenuation can be detected by the chip? First of all, we define the dimensionless variables

$$i = \frac{I}{I_0} \tag{2.21}$$

and

$$\bar{\alpha} = -\ln i \tag{2.22}$$

According to 2.4 we have

$$i = \exp(-\bar{\alpha}) = \exp\Big(-\int_S \alpha((\vec{x}))ds\Big) \tag{2.23}$$

Now we see by comparison of 2.23 with equation 2.6 that $\bar{\alpha}$ is the projection value needed for the tomographic reconstruction. The error for this value is

$$\Delta\bar{\alpha} = \frac{\Delta i}{i} = \frac{R_n}{I}\sqrt{1+\frac{I^2}{I_0^2}} \tag{2.24}$$

Table 2.2 shows error levels for i and $\bar{\alpha}$ for a 12bit camera with given noise level R_n. Displayed are some typical values for a tomography application. I_0 will typically use the full range of the camera. However, the beam intensity may not be constant over the surveyed area, and lower values for I_0 must be accepted. We see from table 2.1 that this fact limits the size of the sample objects if we want to get reliable values for $\bar{\alpha}$. For an attenuation of 1/1000 we have $\bar{\alpha}$= 6.9. Using the full dynamic range of the CCD camera, we can determine this value only to a precision of ±0.25 with $R_n = 1$.

I	I_0	$i = I/I_0$	Δi		$\bar{\alpha} = -\ln i$	$\Delta\bar{\alpha}$	
			$R_n = 1$	$R_n = 4$		$R_n = 1$	$R_n = 4$
4000	4000	1	3.5×10^{-4}	1.4×10^{-3}	0	3.5×10^{-4}	1.4×10^{-3}
400	4000	10^{-1}	2.5×10^{-4}	10^{-3}	2.3	2.5×10^{-3}	0.01
40	4000	10^{-2}	2.5×10^{-4}	10^{-3}	4.6	2.5×10^{-2}	0.1
4	4000	10^{-3}	2.5×10^{-4}	10^{-3}	6.9	0.25	$1 \to \infty$
1	4000	2.5×10^{-4}	2.5×10^{-4}	10^{-3}	8.3	$1 \to \infty$	$4 \to \infty$
400	400	1	3.5×10^{-3}	1.4×10^{-2}	0	3.5×10^{-3}	1.4×10^{-2}
40	400	10^{-1}	2.5×10^{-3}	10^{-2}	2.3	2.5×10^{-2}	0.1
4	400	10^{-2}	2.5×10^{-3}	10^{-2}	4.6	0.25	$1 \to \infty$
1	400	2.5×10^{-3}	2.5×10^{-3}	10^{-2}	6.0	$1 \to \infty$	$4 \to \infty$

Table 2.2: Errors for i and $\bar{\alpha}$ for a 12bit camera with noise level R_n. The errors calculated with 2.24 are not correct for very low count rates. In fact i = 0 lies within the error limits of i, where $\bar{\alpha}$ is infinite. This is indicated in the table by $\to \infty$.

Is it possible to combine multiple exposures with different exposure time to one image with arbitrary dynamic range?

Yes, with a camera, that supports anti-blooming. Otherwise, the surplus of charge in the high intensity areas will spread to the neighboring pixels.

If the intensity to be measured contains values from 10^3 to 10^9 in various regions one could combine, for example, three exposures with different exposure times to see the intensity ranges $10^1 - 10^4$, $10^3 - 10^7$ and $10^6 - 10^9$ separately. The medium exposure image will have overflows in the regions with higher intensity and show only noise in the lower regions. This method is limited by the amount of light in the overflow regions that will kill the camera.

Is it possible to increase the accuracy for $\Delta I/I$ with a camera of given dynamic range by integrating over a large number of exposures?

No. Figure 2.5 illustrates the problem.

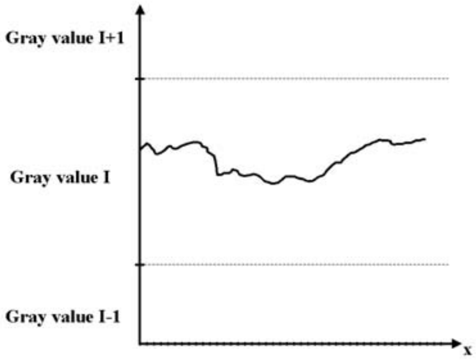

Figure 2.5: The signal differences to be measured are smaller than the discrimination by the camera

One could think that with a camera that has a dynamic range of 10^3 and a noise level of 1 count it should be possible to combine 1000 exposures to measure an I_{tot} of 10^9 with an accuracy of

$$\begin{aligned} \Delta I_{tot} = \sqrt{\Delta I_1^2 + \ldots + \Delta I_{1000}^2} &= \sqrt{1000}\Delta I = 31.6\Delta I = 31.6 \times 1/1000 I = 3.16 \times 10^4 \\ &= 3.16 \times 10^{-5} I_{tot} \end{aligned} \tag{2.25}$$

This will not necessarily work here. The reason is that the errors are not statistically independent, but clearly systematic.

2.3.4 Time resolution

The question of time resolution is identical with the question, what exposure time is needed to measure a certain difference of attenuation $\Delta I/I_0$ with a given accuracy. Usually one wants to measure as high a dynamic range as possible. Thus we need to calculate the time it takes to fill the dynamic range of the camera using the relation

$$\text{countrate} = \text{camera sensitivity} \times \text{incoming photons} \tag{2.26}$$

where we use the definition of the camera sensitivity given in section 2.4. If we have the count rate, the exposure time is just

$$\text{exposuretime} = \frac{\text{dynamicrange}}{\text{countrate}}. \tag{2.27}$$

Geometrical considerations

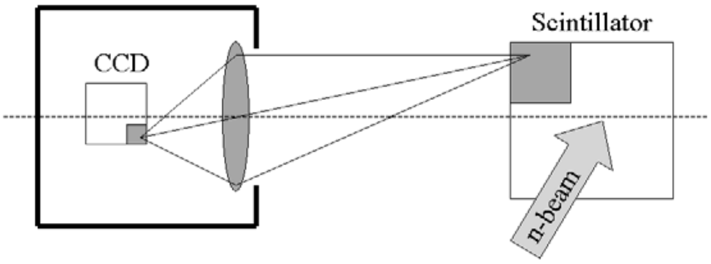

Figure 2.6: General optical system

We calculate now the number of photons hitting the CCD chip when a single neutron is detected in the scintillator. We assume that the aberrations of the optic are smaller than a pixel and all the light emitted by the conversion of a neutron on the scintillator hit the same pixel. If aberration plays a role further corrections must be introduced! For the solid angle ω of the lens seen by a point on the scintillator we have

$$\omega = \frac{A_{lens}}{4\pi L^2} = \frac{d_{lens}^2}{16L^2} \tag{2.28}$$

where L is the distance between lens and scintillator and d_{lens} is the diameter of the lens. This is exactly the portion of the photons emitted by the scintillator that reach the CCD camera.

$$\frac{dN_{\text{photon,ca}}}{dn} = \frac{d_{lens}^2}{16L^2}\frac{dN_{\text{photon,sc}}}{dn} \tag{2.29}$$

The rate of photons that reach one single CCD pixel depends further on the intensity of the neutron beam $I_{n,0}$ on the scintillator, the probability of one neutron to be detected by the scintillator $P_{n,sc}$ and the area on the scintillator that corresponds to one CCD pixel (which will subsequently be called the scintillator pixel) $A_{p,sc}$ indicated in figure 2.6.

$$\frac{dN_{\text{photon,ca}}}{dt} = \frac{d_{lens}^2}{16L^2} \times \frac{dN_{\text{photon,sc}}}{dn} \times P_{n,sc} \times A_{p,sc} \times I_{n,0} \tag{2.30}$$

How can the exposure time be minimized and how is this expressed in terms used by camera and optics manufacturers?

Most obviously we want a high neutron flux and a very efficient scintillator with high light output. However, these factors are usually given and we have to optimize the rest of the system.
Objectives, just like lenses, are characterized by their focal length f and their $f/\#$ (pronounced "f-number"), which is defined by

$$f/\# = \frac{f}{d} \tag{2.31}$$

where d is the diameter of the maximum lens aperture. $f/\#$ is larger than 1.0 for almost all objectives meaning that it's almost impossible to make d larger than f. The aperture area can be expressed in terms of $f/\#$ and f

$$A_{Aperture} = \pi\Big(\frac{d}{2}\Big)^2 = \pi\Big(\frac{f}{2f/\#}\Big)^2 \tag{2.32}$$

Since the amount of light collected by the lens is proportional to the area of the lens aperture $\pi(\frac{d}{2})^2$ and $f/\#$'s are greater than 1.0, a big maximum aperture area requires a large focal length.

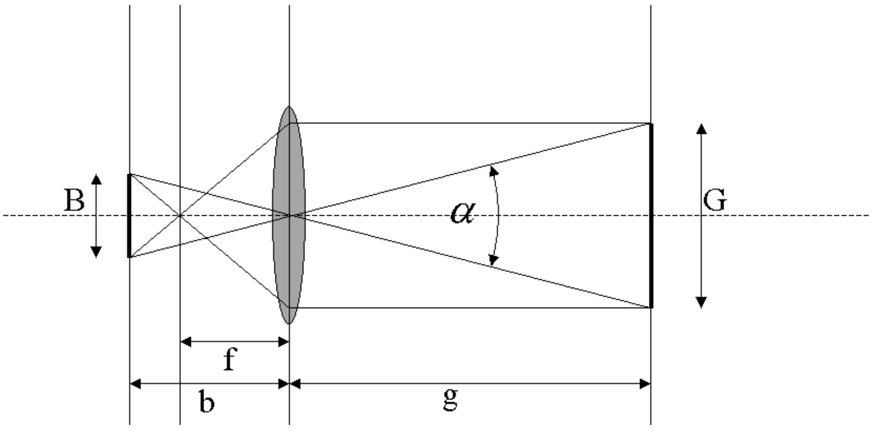

Figure 2.7: Lens principle

The choice of CCD chip and objective is determined by some physical relations. First of all we have the thin lens equation

$$\frac{1}{b} = \frac{1}{f} - \frac{1}{g} \tag{2.33}$$

from which we find the image distance

$$b = f\frac{g}{g-f} = f\frac{1}{1-f/g} \tag{2.34}$$

b is usually close to f as long as g ≫ f, which can also be seen from figure 2.7. Furthermore, we have the simple relation

$$\frac{B}{b} = \frac{G}{g} \tag{2.35}$$

which is quite obvious from figure 2.7 if we consider just the light rays through the center of the lens, which are not diffracted at all. We can use 2.35 to eliminate b from 2.33 and write

$$f = \frac{g}{1+\frac{G}{B}} \tag{2.36}$$

The angle α seen by the camera is given by

$$\tan(\frac{\alpha}{2}) = \frac{G}{2g} = \frac{B}{2b} = \frac{B}{2f}(1 - f/g) \tag{2.37}$$

If we know that G is significantly larger than the chip size B, we have from 2.36 a rough estimation for the relation between B and f for the system we are going to build.

$$\frac{B}{f} \approx \frac{G}{g} = 2\tan(\frac{\alpha}{2}) \tag{2.38}$$

On the other hand, if the chip size B and the objective parameters are given, one can compute the solid angle 2.28 of the maximum aperture in terms of the visible object size (figure 2.8) by using 2.32 and 2.36.

$$\omega = \frac{1}{4\pi g^2}\pi\Big(\frac{f}{2f/\#}\Big)^2 = \frac{1}{16(f/\#)^2(1+\frac{G}{B})^2} \tag{2.39}$$

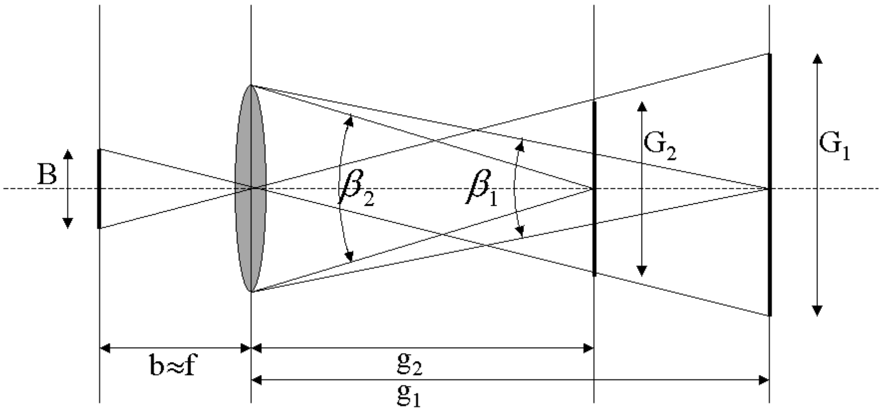

Figure 2.8: Solid angle of the lens for varying object sizes

The size of the scintillator pixel defined above is with the CCD array dimensions M_x, M_y

$$A_{p,sc} = G_x/M_x \times G_y/M_y \tag{2.40}$$

Together with the neutron intensity on the scintillator $I_{n,0}$, the detection probability of the neutrons on the scintillator $P_{n,sc}$, the size of the scintillator pixel 2.40 and the formula for the camera sensitivity in counts per photon, that will be derived in section 2.4, we find the complete expression for the count rate in one pixel depending on what kind of information is given by the camera producer (the symbols are explained in section 2.4).

$$countrate[s^{-1}] = I_{n,0}[cm^{-2}s^{-1}]P_{n,sc}\tfrac{dN_{ph}}{dn}\tfrac{G_x[cm]}{M_x}\tfrac{G_y[cm]}{M_y}\tfrac{1}{16(f/\#)^2(1+\frac{G}{B})^2} \times \text{binning} \times \text{gain}\times \\ \begin{cases} QE_{ca} \times \text{fill factor} \times \dfrac{\text{DAC range}}{\text{full well capacity}[\text{e}^-]} \\ QE_{ca} \times \text{fill factor} \times \Big(\text{conversion factor}\Big[\frac{e^-}{count}\Big]\Big)^{-1} \\ \frac{3.58\times10^{-13}}{(B_x[cm]B_y[cm])/(M_xM_y)} \times \text{R}_E\Big[\dfrac{\text{counts}}{\mu\text{J}/cm^2}\Big] \\ \frac{2.45\times10^{-12}}{(B_x[cm]B_y[cm])/(M_xM_y)} \times \text{R}_L\Big[\dfrac{\text{counts}}{\text{lux s}}\Big] \end{cases} \tag{2.41}$$

Together with the dynamic range of the camera this yields directly the exposure time according to equation 2.27. B_x, B_y and G_x, G_y are, of course, not completely independent but constrained by the relation

$$\frac{G_x}{G_y} = \frac{B_x}{B_y} \tag{2.42}$$

Thus, G/B is the same for both directions and the indexes are left away in equation 2.41 where the distinction is not necessary.

The focal length is further determined by the experimental conditions g and G and the choice of the chip size according to 2.36. With equation 2.41 we can now compare CCD cameras in terms of the expected exposure time for a given problem, depending on the properties of the chip and the objective.

2.4 Characteristics of CCD cameras

A charge coupled device (CCD) chip converts photons to electric charge. An incoming photon produces a free electron in the sensitive layer of the chip when it is detected. Each pixel collects electrons over a certain exposure time and is then evaluated by an analog digital converter (ADC). For an overview of the CCD principle see [Au201]. For a very good explanation of various CCD camera properties see the "CCD Primer" and the "Technical Notes" at [Rop01]. Here is a short overview of the most important CCD camera features:

Chip and pixel size	In this context we are interested in array sizes from 512x512 to 1280x1280 according to the expected resolutions. Common chip diagonals are 1/3" 1/2", 2/3" and 1" depending on the array and pixel size. Pixel sizes range from 4.95μx4.95μ to 20μmx20μm. Cameras with smaller pixels are often faster.
Chip type	*Progressive scan.* Complete frame readout as opposed to interlaced readout that reads out odd and even lines alternately. *Full frame.* Shifts the whole image to the one edge of the chip where it can be read out line by line. During readout pixels are still exposed. A shutter is required to avoid artifacts due to this circumstance. *Frame transfer.* Puts the whole image very fast in an on chip buffer at the end of exposure time. For frame transfer chips there is a minimum exposure time of several milliseconds. For shorter exposure times an additional shutter is required. *Transfer line.* Storage and detection happen at the same place. The fill factor is small because the pixels contain elements for storage and detection. Lens on chip architecture reduces this problem by focusing the light on a pixel to the sensitive area.
Fill factor	Between the sensitive area of the pixels there can be non sensitive zones on the CCD chip. The ratio of the sensitive area to the chip area is called fill factor. Cameras with fill factor 100% are available. Usually this value is around 80%.

Quantum efficiency QE	The probability of a photon to be detected when it hits the sensitive area of the chip. It is the ratio of produced electrons to the number incident photons on the sensitive area. The typical range is 20% -80%, usually cameras have about 40%.
Full well capacity	The amount of electrons that can be stored on a CCD pixel before it saturates. (for example 45000 e$^-$ for a Kodak KAF1400 chip with $6.8\mu m \times 6.8\mu m$ pixels). It depends almost linearly on the pixel area. The ratio of the full well capacity to the noise level in electrons is the limitation for the effective dynamic range of the chip.
Conversion factor / gain	The conversion factor or gain describes how many electrons are necessary to produce one count. While the conversion factor gives this information directly in e^-/count, $gain = 1$ means that the full range of the ADC matches the full well capacity of the chip. Thus the rate of photons per count usually depends on the chip size. Typically, the available gain value is in the range of 1 to 4. In most cases the user can choose between at least two gain values.
Signal to noise ratio S/N	The full range of the camera readout, for example 4096 counts with 12 bit digitization, can generally not be used because of noise effects. There are two types of noise. This is read out noise and thermal noise. Read out noise is a fixed value and does not depend on the exposure time. It is usually between 1 and 4 counts per pixel. Thermal noise accumulates during exposure time. Typical values are about 1-4 counts per second and pixel. Sometimes it is given in terms of electrons rather than counts and called dark current. 12bit cameras with image intensifiers and high gain have about 15 counts per second of thermal noise. The noise depends on the camera gain or conversion factor. High gain will also increase the thermal and readout noise level. For short exposure times, thermal noise is well below readout noise with standard gain settings. The effective dynamic range is the ratio of the dynamic range of the output signal to the noise level.
Readout speed	Most of the cameras with array sizes of about 1024x1024 and 12 bit digitization can read out about 10 to 30 full frames per second. The limiting factors are the time required by the ADC and the connection used for transporting the data out of the camera.

Binning	A number of pixels on the chip (2x2, 4x4, etc.) are treated as one large pixel. All CCD cameras allow for binning. It increases the readout speed since a smaller number of lines must be transported to the evaluating register and less digitizations must be performed. 2x2 binning increases readout speed by slightly less than a factor of 2. Binning doesn't increase the readout noise! A 4x4 binned big pixel should have the same readout noise as a single pixel in full resolution mode. The signal to noise ratio is improved by a factor equal to the number of binned pixels.
Trigger and shutter accuracy	With standard cameras down to μs available. However, not with all cameras.
Anti blooming	When the full well capacity is reached the pixel saturates. Further produced electrons drift to the neighboring pixels. Anti blooming avoids this effect.

We can define the camera sensitivity in terms of the number of counts produced for a given number of incident photons.

$$\text{camera sensitivity} = \text{counts/photon} \tag{2.43}$$

The following units are sometimes used by camera manufacturers to specify the sensitivity of their cameras. They are defined for green light with wavelength 555nm:

1 cd = 1/683 Watt/sr
1 lumen = 1/683 Watt
1 lux = 1/683 Watt/m^2

We rather express the units watt and lux in number of green photons using hc/555nm = 2.24eV. The resulting values apply to a scintillator with green light output.

1watt = $6.24 \times 10^{18} eV/s = 2.79 \times 10^{18}$ green photons/s
1lux = 4.08×10^{15} green photons $/m^2 s$

The camera sensitivity is sometimes described by the camera producers in counts/(μJ/cm^2) or counts/(lux s). These values are then, for example, called responsivity. We denote these R_E and R_L, respectively. However, if these units are used, it is very important to look at the exact definition of the measurement given by the producer. There can be large differences! Often, the values are defined for a certain light source with given spectrum. For further information on the unit lux see [Rei01]. For the discussion of the special case of a Kodak KAF-0400 chip, see [Au301]. It has further to be verified, that the given light intensities are measured on the chip, rather than on a reference object.
From these definitions we can derive the desired camera sensitivity in counts per green photon.

$$\begin{array}{c}\text{camera sensitivity}\\ \text{[counts/photon]}\end{array} = \begin{cases} QE_{ca} \times \text{fill factor} \times \dfrac{\text{DAC range}}{\text{full well capacity}[\mathrm{e}^-]} \\ QE_{ca} \times \text{fill factor} \times \left(\text{conversion factor}\left[\frac{e^-}{count}\right]\right)^{-1} \\ \frac{3.58\times10^{-13}}{(B_x[cm]B_y[cm])/(M_x M_y)} \times \mathrm{R}_E\left[\dfrac{\text{counts}}{\mu\text{J}/cm^2}\right] \\ \frac{2.45\times10^{-12}}{(B_x[cm]B_y[cm])/(M_x M_y)} \times \mathrm{R}_L\left[\dfrac{\text{counts}}{\text{lux s}}\right] \end{cases} \tag{2.44}$$

(2.45)

We keep in mind that the factors used together with R_E and R_L hold only for green photons and can at most be seen as a very rough estimation in other cases. B_x, B_y are the chip dimensions in cm, M_x M_y are the numbers of pixels in either direction. The expression for the pixel size $B_x[cm]B_y[cm]/(M_xM_y)$ can be replaced by $10^{-8}A_{pix}[\mu m^2]$. The notation in terms of the chip size and the array size was used, because the considerations in section 2.3.4 use these values rather than the direct pixels size. The sensitivity of the camera can further be modified by setting the gain value. The indicated values usually hold for the setting gain = 1. Binning does, of course, not increase the response per photon, but effectively increases the count rate. The count rate of the binned pixel is just the sum of the count rates of the single pixels when run in full resolution mode.

2.5 Representation of tomography data

The most straightforward way to visualize a reconstructed three dimensional object is to scroll through it slice by slice. The implementation is quite easy and can as well be found on standard software packages.

A more advanced manner of visualizing volume data is to create a 3d model, for example with VGStudioMax from VolumeGraphics [Vol01]. A three dimensional model often permits a better understanding of the reconstructed data than just scrolling through the slices. Segmentation, furthermore, allows to view single components while blinding out all the rest of the volume that is of less interest. A lot of examples are shown in chapter 3.

Chapter 3

Measurements at the Pf1b cold neutron beam of the ILL

3.1 Overview

At the cold neutron beam Pf1b, it was possible to install a temporary setup for tomography well before the tomography station at the H9 was ready for measurements. The tomography measurements were performed behind the PERKEO experiment, which measures parameters of the weak interaction in the neutron β-decay (see [Mun00]). The neutron flux of Pf1b is $1.6 \times 10^{10} n/cm^2 s$ direcly at the beam exit. Due to the present polarization and collimation system, a well collimated beam of flux $5 \times 10^7 n/cm^2 s$ was available for the tomography. The setup was placed 9m from the exit of the polarizer.
The beam was available for the tomography only for a limited period but allowed first experiments for testing and developing the reconstruction algorithm. Useful experience on handling of the samples, the setup components and the resulting data could be gained. The availability of experimental data in such an early stage of the project allowed familiarization with the possibilities and advantages of the technique, practical limitations, artifacts, available software and representation of the reconstructed object data. Despite the high flux at the Pf1b beam line, the temporary setup was not yet suited for fast measurements with sub-second exposure times as they are planned for H9 .

Even though there is no tomography station yet, a fair amount of practical experience is at hand. Without having finished the actual facility, first neutron tomography results can be presented.

3.2 The test samples

A set of simple objects was used for testing the image acquisition and reconstruction methods.

- A block with the dimensions 3x3x4cm^3 with a large hole and thread lengthwise for a M16 screw and an additional hole of diameter 1cm perpendicular to the thread. The thread hole is broadened on the upper side to incorporate the screw head
- A pan head sloted M16 screw of length 4cm
- In some cases an aluminum plate of thickness 1mm was wrapped around the sample to give the sample more detail

The screw and the block are available of aluminum, steal and plastic and were used in several combinations. Figure 3.1 shows a drawing of the sample parts. Figure 3.2 and 3.3 show reconstruction previews of block and screw both of aluminium (figure 3.2) and of the steal screw in the aluminum block with the aluminum plate wrapped around (figure 3.3).

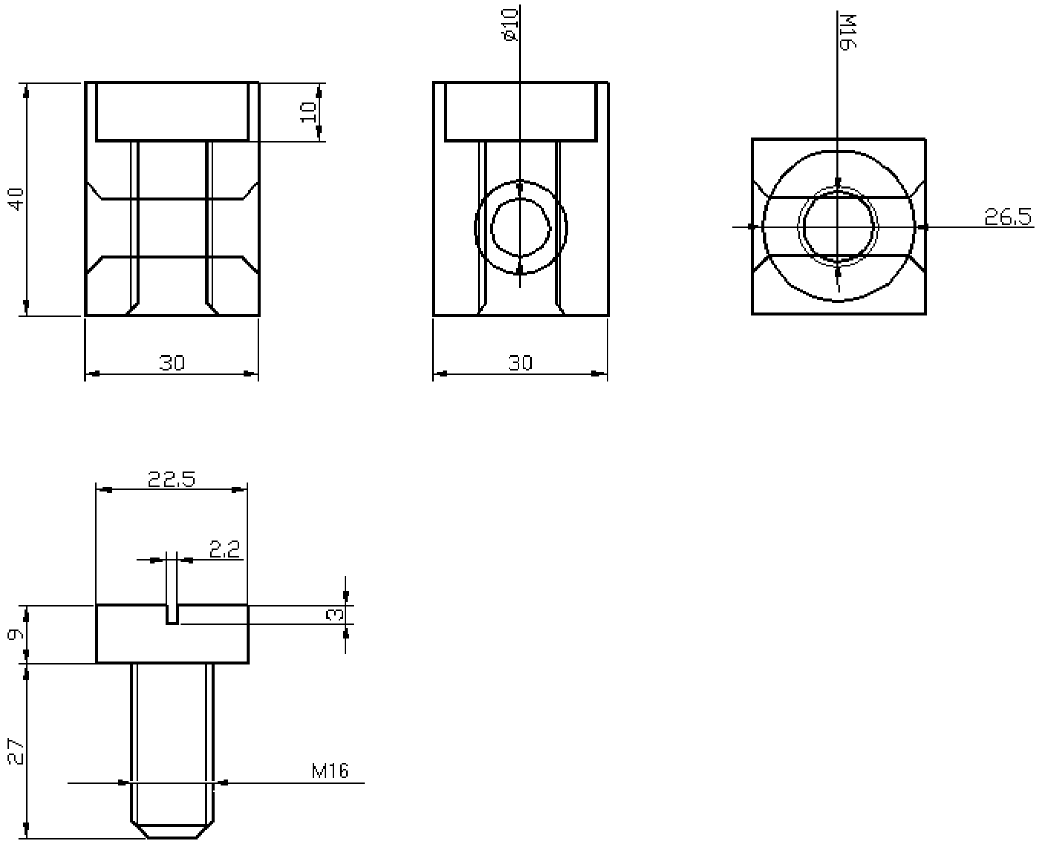

Figure 3.1: The test sample parts

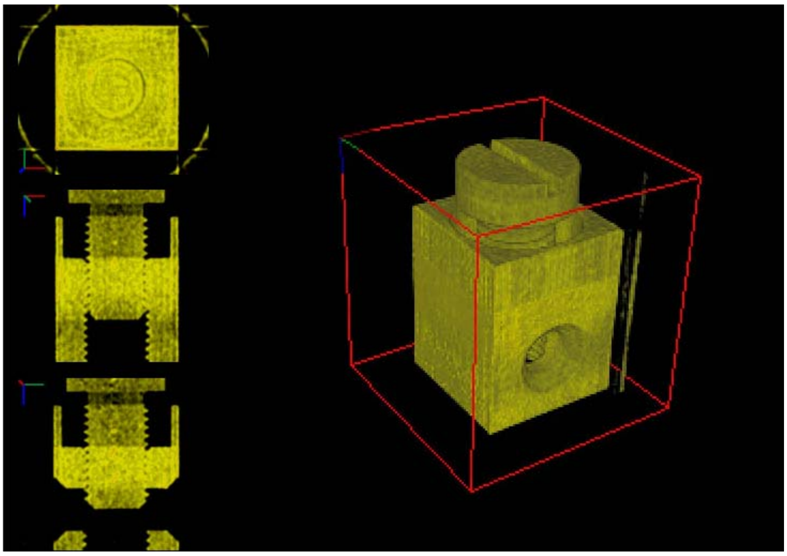

Figure 3.2: 3D model (right) of a reconstructed test sample and slices of various orientations (left). Screw and block are of aluminum.

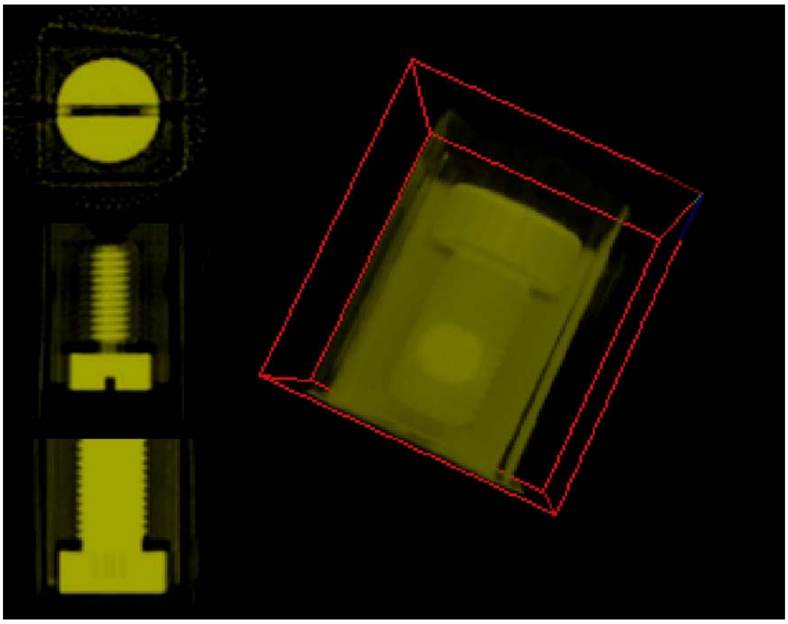

Figure 3.3: Transparency model of a steal screw in an aluminum block with an aluminum plate wrapped around. The steal screw is visible inside the aluminum parts. The steal screw attenuates the neutron beam stronger than the aluminum parts and is represented by higher gray values.

3.3 Properties of the image acquisition system

3.3.1 Neutron beam

The tomography experiment was installed temporarily behind the PERKEO experiment. With the existing system for polarisation and collimation the Pf1b cold neutron beam provides a flux of $5 \cdot 10^7 n/cm^2 s$ neutrons at the position of the tomography experiment. At the beam exit, the unpolarized beam has an intensity of $1.6 \times 10^{10} n/cm^2 s$ with a 6cm × 20cm (w × h) cross section of the neutron guide. The mean neutron velocity is 780m/s. The exit of the polarizer with cross section 2.7cm × 4.5cm can be seen as the source for the tomography setup in 9m distance. Thus, the horizontal and vertical L/D ratio for the tomography is 333 and 200 respectively, making the tomography setup comparable with the best tomography stations so far, for example at the PSI, but with higher flux. The expected horizontal resolution for the this L/D ratio is 0.3mm for a distance of 10cm between sample and scintillator, which was verified experimentally. The L/D ratio of 333 corresponds to 3mrad divergence.

The profile of the beam intensity within an area of 5.7x8.5cm is shown in figure 3.4. The intensity falls to about one fourth of its maximum value at the upper and lower end of the 8.5cm visible height. To the left and right it falls to about one third of the maximum value within the visible width of 5.5cm. Further details about the Pf1b beam can be found in [Mun00].

3.3.2 Camera, optical system and scintillator

The scintillator and the CCD camera are contained in a closed system to avoid any other light than from the scintillator to reach the CCD chip. The simplest way to do this would be to place the camera right before or after the scintillator. The camera would then be in the beam and be disturbed, activated or even destroyed by the incident neutrons or gamma radiation. It is therefore preferable to have the camera watch the scintillator via a mirror. The setup shown in figure 3.5 has another mirror in the joint, which was originally added to make the whole device more flexible. It also proved useful for the shielding of the camera. The joint allowed to place

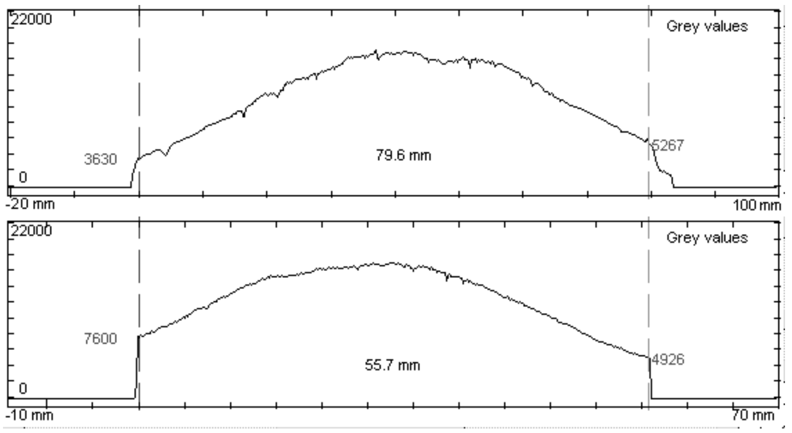

Figure 3.4: Vertical (upper picture) and horizontal (lower picture) distribution of the beam intensity within the visible area of 8.5cmx5.5cm. The intensity is given in counts of the CCD camera along the middle of a reference image of the beam. The maximum corresponds to $5 \cdot 10^7 n/cm^2 s$

lead and boron shielding between the camera and those parts which are directly in the beam (see figure 3.8). The camera and scintillator system was designed, built and made available for these measurements by A.Heidemann (ILL).

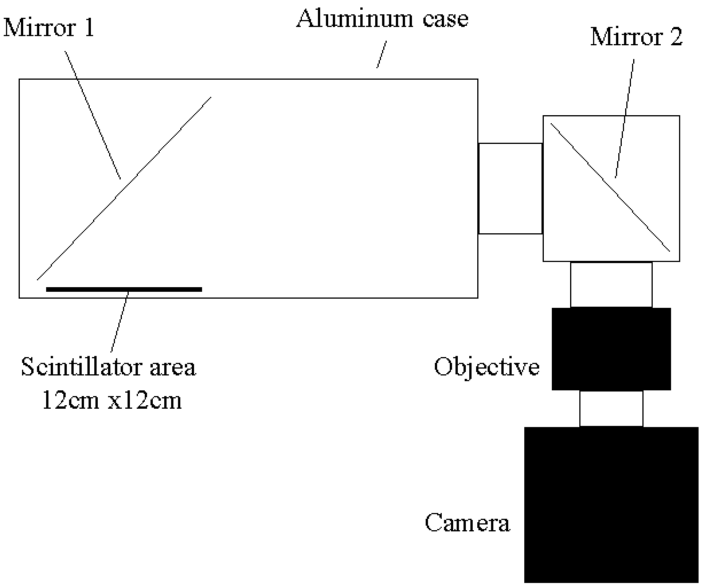

Figure 3.5: Camera and scintillator box

The AUDINE CCD camera is a product of the AUDINE project of the Association des Utilisateurs de Détecteurs Electroniques (AUDE), originally designed for astronomic observations and suited to the needs of amateur astronomers. Its general properties are listed below. All information on AUDINE as well as camera software and programming manuals can be found at the AUDINE projects web page [Aud01].

Number of pixels	768 × 512
Dimensions of the pixel	9 × 9 μm^2
Dimensions of the sensitive surface	6.9 × 4.6 mm^2
Fill factor of the pixel	100%
Full well capacity	82000e$^-$
Average quantum efficiency	35%
Noise	see section 3.3.5
Output	16bit (only 15bit are used!)

Because the AUDINE camera has no shutter, the CCD chip must not be exposed to light during the readout process. This would lead to artifacts in the image. As output format of the AUDINE camera the Flexible Image Transport System (FITS) file type developed by NASA was chosen. A detailed description of the FITS format as well as software packages and code libraries for manipulating FITS files are available for download at [Nas01].
Due to the used camera objective a section of the scintillator of $5.7cm \times 8.5cm$ was visible according to a pixel resolution of

$$1cm = 90 \pm 1 \quad \text{pixel} \tag{3.1}$$

An objective with a focal length of 28mm and a maximum aperture number of 2.8 (f/#) was used. The scintillator is sensitive not only to neutrons, but also to gamma rays. The maximum of the emitted photon spectrum is at 560nm (green light). The exact specification of the scintillator was not available. It is reasonable to assume a detection probability of 0.2 for the neutrons on the scintillator and a light output per neutron of 10^5 photons.

3.3.3 Image acquisition

The AUDINE cameras output format is 16bit. However, only 15 bit are used. All images taken by the AUDINE camera have an offset of about 6000 counts, that must be subtracted from the projection images. It is furthermore useful to keep the maximum signals well below the overflow value. Thus, a dynamic range of 20000 counts is left. To use this dynamic range with the given scintillator setup and beam intensity an exposure time of 20 sec per image was necessary. With this information it is possible to test the formula derived in section 2.3.4. Using $f/\# = 2.8$ for the objective, $P_{n,sc} = 0.2$ for the detection probability of the scintillator and 10^5 photons for its light output per neutron, the count rate without binning and with standard gain (the AUDINE camera doesn't allow any gain settings) becomes according to equation 2.41

$$\begin{gathered}
\text{countrate}[s^{-1}] = I_{n,0}[cm^{-2}s^{-1}]P_{n,sc}\tfrac{dN_{ph}}{dn}\tfrac{G_x[cm]}{M_x}\tfrac{G_y[cm]}{M_y}\tfrac{1}{16(f/\#)^2(1+\frac{G}{B})^2}\times \\
QE_{ca} \times \text{fill factor} \times \frac{\text{DAC range}}{\text{full well capacity[e}^-]} \\
= 5 \times 10^7 \times 0.2 \times 10^5 \times 8.5/768 \times 5.7/512\times \\
(16 \times 2.8^2(1+8.5/0.69)^2)^{-1} \times 0.35 \times 1 \times \tfrac{32767}{82000} = 770
\end{gathered} \tag{3.2}$$

With the used dynamic range of 20000 counts this gives

$$\text{exposuretime[s]} = \frac{20000}{980} = 26.0 \tag{3.3}$$

Considering the very rough estimation of the scintillator properties, the result is acceptable compared to the actual exposure time of 20s.
The total setup, as shown in figure 3.8, was designed in a way, that other detectors like image plates could as well have been used. Rather than an optical shutter between the scintillator and the camera, a moving slit aperture of 5mm boron and 10cm lead was used to have a defined and reproducible amount of neutrons on the detector during exposure time. The sample holder with the rotary stage is shown in figure 3.7. To drive the camera the AUDINE cameras standard software Pisco was used. It allows automatic capture of a series of images with adjustable exposure time and delay. A second little program just checked for the presence of the read image in the

destination folder of the PC to start the movement of the linear and rotary stage for the next exposure. Figure 3.6 shows the principle of the measurement.

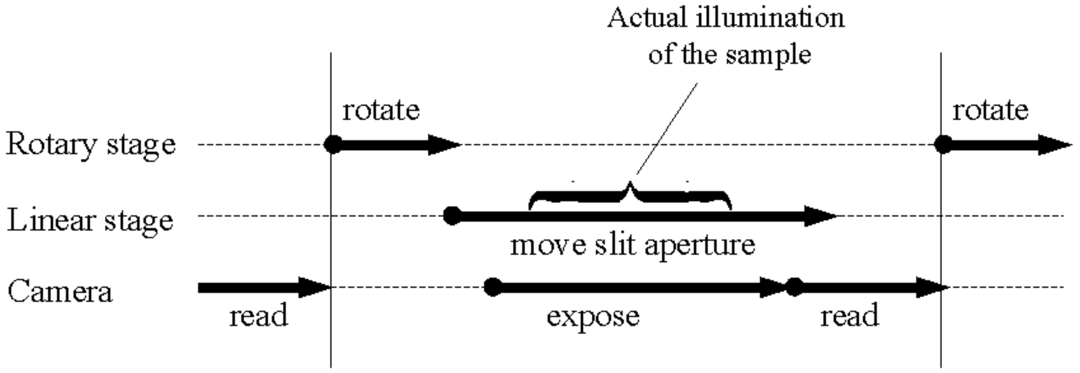

Figure 3.6: Principle of the measurement

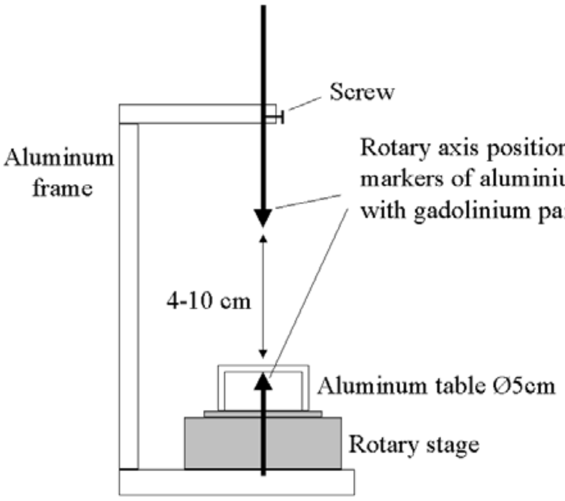

Figure 3.7: Sample holder with rotary stage and rotary axis position markers

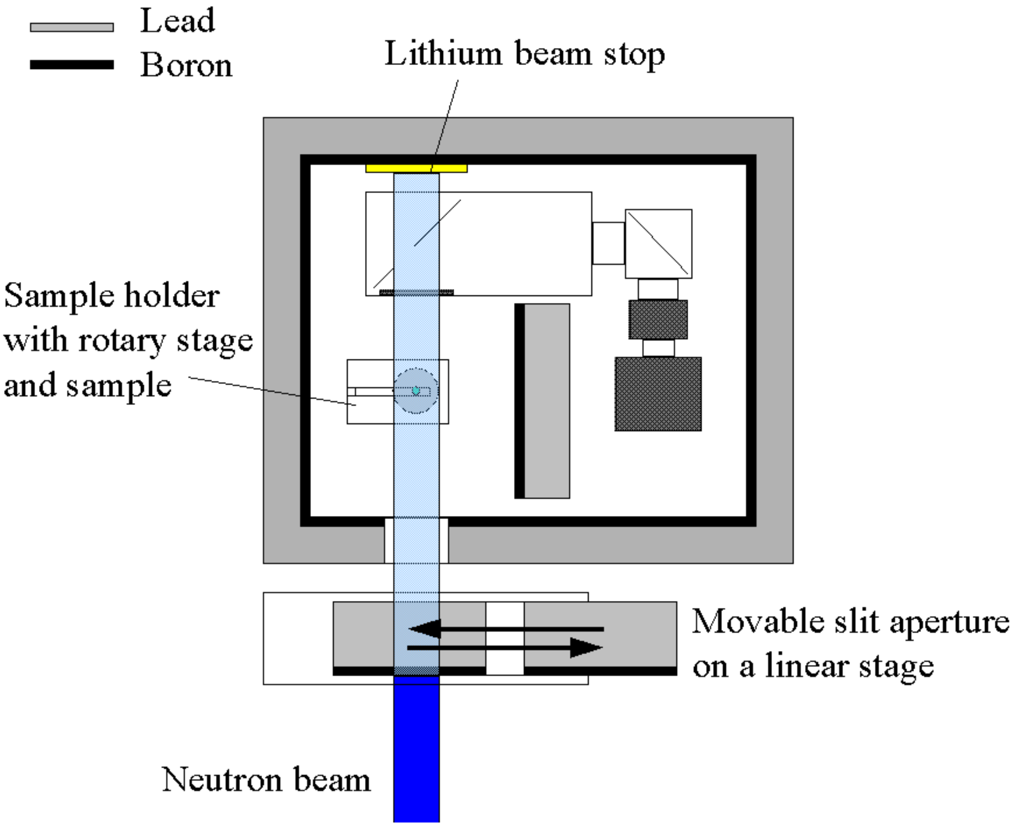

Figure 3.8: Image acquisition setup

A lithium beam stop was used to avoid the production of gamma rays close to the detector. Without the lithium beam stop, the neutrons are stopped by the boron layer behind the scintillator case. Tests showed that the lithium beam stop reduces notably the gamma background on the taken images.

3.3.4 Preparation of the projection data

The camera offset of the AUDINE camera must be subtracted from all the projection images. The value of interest is the factor by which the intensity is reduced by the sample. Thus, the projection images have to be divided by a reference image of the full beam without sample. The reference image has to be corrected for the camera offset as well. The camera offset image was acquired with the neutron beam switched off and by choosing the shortest exposure time possible to avoid thermal noise. Readout noise, however, couldn't been avoided this way.

Positioning of the camera was not accurate enough to have the rotary axis of the sample match exactly one column in the projection images. In general, it was necessary to tilt the projections. The region of interest was cropped from the tilted projections so that the rotary axis was represented by the middle of the cropped images. This operation was automated using the Intel Performance Library for Image Processing (IPLib, see [Int01]) because the same set of operations had to be performed for the complete set of projections (for example 180).

A check for the correct position and orientation of the rotary axis can be performed by subtracting the normalized projections at 0 and 180 degrees (therefore it is useful to take the 180° image even though it is not used for reconstruction) one of which flipped about the assumed rotary axis. The squared difference image has a minimum when the correct axis position and orientation is found.

The normalized projection images were stored logarithmic since these are the values needed by the reconstruction algorithm. The resolution of the projection images is 0.3mm (see section 3.7)

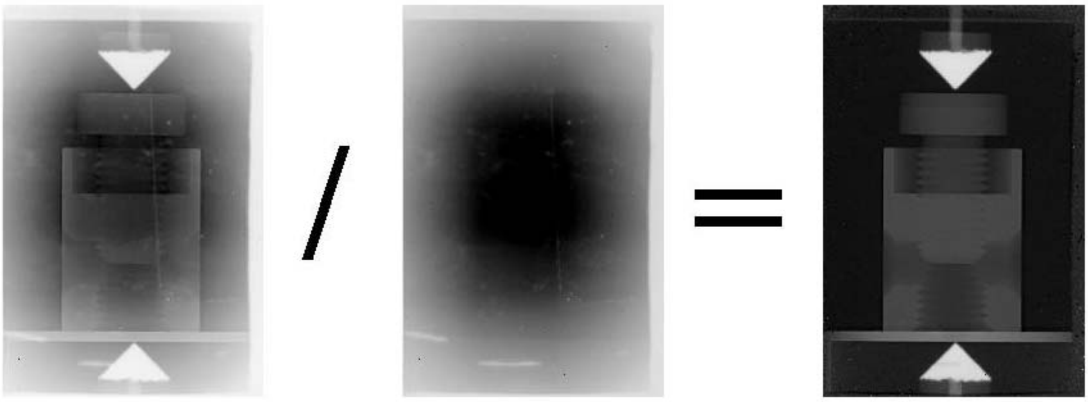

Figure 3.9: Preparation of the projection data

3.3.5 Sources of error

With the long exposure time of 1 minute (for 20 sec illumination of the sample according to the setup properties), there is a lot of thermal noise in the images taken with the AUDINE camera. It is almost 100 counts as shown in figure 3.11. This is well above the readout noise of about 10 counts shown in figure 3.10. The errors for the measured values have to be determined from 2.24.

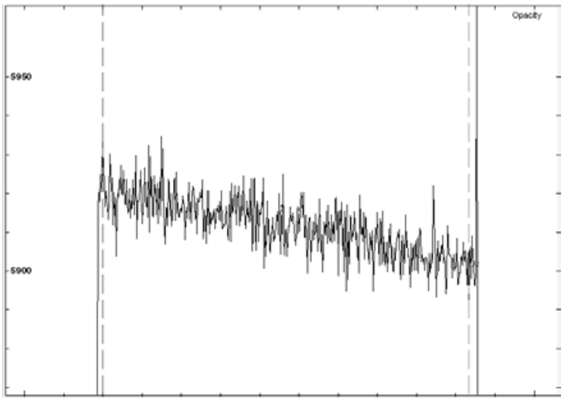

Figure 3.10: Camera offset with readout noise of the AUDINE camera determined with the shortest exposure time available (<1s). Gray values along the image diagonal. The decrease to the right is due to the camera offset.

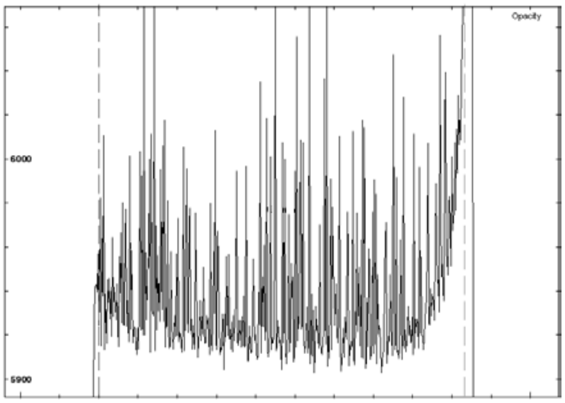

Figure 3.11: Camera offset with thermal noise of the AUDINE camera for an exposure time of 60s. Gray values along the image diagonal.

The sample objects are situated in the middle of the surveyed area. Therefore, we assume I_0 to be 20000 counts for all measurements. the resulting error levels are displayed in table 3.1.

I	$i = I/I_0$	Δi	$\bar{\alpha} = -\ln i$	$\Delta\bar{\alpha}$
20000	1	7×10^{-3}	0	7×10^{-3}
10000	0.5	5×10^{-3}	0.69	0.01
5000	0.25	5×10^{-3}	1.39	0.02
2000	0.10	5×10^{-3}	2.30	0.05
1000	0.05	5×10^{-3}	3.00	0.1
500	0.025	5×10^{-3}	3.69	0.2
200	0.010	5×10^{-3}	4.61	0.5
100	0.005	5×10^{-3}	5.30	$1 \rightarrow \infty$

Table 3.1: Errors for the relative intensity i and the measured attenuation coefficient $\bar{\alpha}$ for the AUDINE camera with thermal noise of 100 counts according to 1min integration time and with $I_0 = 20000$ counts.

We can use this table or equations 2.20 and 2.24 to find the errors. Apart from the errors derived in section 2.3.3 there are further sources of error arising from the experiment setup.

Errors increasing the count rate:

- Scattering of neutrons in the sample. This means that the assumption stated in section 2.1 doesn't hold, and the neutrons scattered by the sample hit the detector, causing an additional offset.
- Production of gamma rays in the object. Gamma rays, produced in the aluminum when the neutrons are absorbed, can cause an additional background on the scintillator.
- Production of gamma rays in the detector, as the neutron beam hits the aluminum walls of the scintillator box, the mirror or a beam stop after the detector. To avoid the latter a lithium beam stop was used which reduced this effect, but could not remove it. It was not possible to avoid the gamma intensity from the aluminum walls and the mirror. For further constructions, close to the scintillator should be as little as possible material that causes gamma intensity. The mirror and the walls of the box must be as thin as possible. In contrast to the effects mentioned before, gamma rays from the detector parts affect the

most the reference image of the full beam causing values < 1 even outside of the object in the normalized images. Since the gamma source is closer to the scintillator in this case, the spacial variation of the effect depends on the distribution of the neutron rate on the screen.

How much exactly these effects contribute to the measured values will have to be specified. General errors:

- Fluctuation of the beam intensity. A change in the beam intensity would cause a parallel shift of the graph according to a constant factor. So far there haven't been any indications for fluctuations of the beam intensity during the measurements.

- Read off errors. High fluctuations of the gray values are found even in areas where the normalized intensity is expected to be constant. The reasons for this are noise and statistical fluctuations as well as the error sources mentioned above. The gray value of a certain area in the images couldn't be determined better than with 1% accuracy. If the errors indicated in the figures are larger than in table 3.1, this is due to read off errors.

3.3.6 Linearity of the measured signals

A simple test was performed to ensure that the camera output of the scintillator and the CCD camera actually goes linear with the number of neutrons that hit the scintillator surface. An image was taken with several exposure times and the count rate in an area with high intensity displayed as function of the exposure time (figure 3.12).
Within the checked exposure time range and the maximum error level of 2% for the lowest count rate, there was no indication of any nonlinearity between neutron rate and count rate.

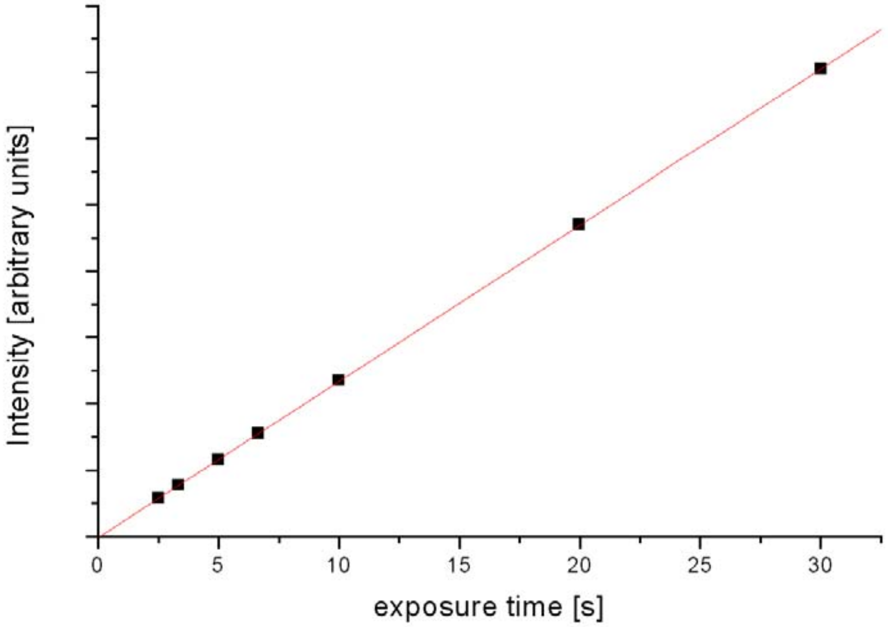

Figure 3.12: Linearity of the image acquisition system. Errors $\leq 2\%$.

3.4 Measurement of beam attenuation with radiographic images

A radiograph of aluminum parts with defined thickness was taken (figure 3.13) and the normalized intensity plotted over the thickness of the aluminum ($\rho_{\text{aluminum}} = 2.7g/cm^3$). According to equation 2.2 and 2.1 the attenuation coefficient of aluminum should be

$$\begin{aligned} \alpha &= (\sigma_{s,i} + \frac{2200\frac{m}{s}}{v_n}\sigma_{a,2200})\rho\frac{N_A}{M_{Mol}} \\ &= (0.0082 + \frac{2200}{780} \times 0.231) \times 10^{-24}cm^2 \times 2.7\frac{g}{cm^3} \times \frac{6.022\times 10^{2}3}{27g} = 0.040cm^{-1} \end{aligned} \tag{3.4}$$

The exponential fit gives an attenuation coefficient of 0.086 ± 0.001. This does not match the expectations. However, the exponential behavior is obvious. The effect can be due to effects from the granular structure of the aluminium. The attenuation properties of aluminium can depend on the way the aluminium was processed. The grain size of the material could in this case cause, for example, small angle scattering effects.

Figure 3.16 shows the result of a similar attenuation measurement with acryl glass $[C_5O_2H_7]_n$ (figure 3.15). Because of the high cross section of H, the other components will not significantly contribute to the attenuation. The expected attenuation coefficient can be derived by considering only the density of H in the material ($\rho_{\text{acryl glass}} = 1.19g/cm^3$).

$$\begin{aligned} \alpha &= (\sigma_{s,i} + \frac{2200\frac{m}{s}}{v_n}\sigma_{a,2200})\rho\frac{N_A}{M_{Mol}} \\ &= (80.3 + \frac{2200}{780} \times 0.33) \times 10{-}24cm^2 \times \frac{7\times 1}{5\times 12+2\times 16+7\times 1}1.19\frac{g}{cm^3}\frac{6.022\times 10^{23}}{1g} = 4.11cm^{-1} \end{aligned} \tag{3.5}$$

The fit gives $4.33 \pm 0.1cm^{-1}$.

One of the normal projection images was used to gain further attenuation data. The attenuation of steal ($\rho_{\text{steal}} = 7.87g/cm^3$) was determined from a projection of the steel screw in aluminium (figure 3.17).

$$\begin{aligned} \alpha &= (\sigma_{s,i} + \frac{2200\frac{m}{s}}{v_n}\sigma_{a,2200})\rho\frac{N_A}{M_{Mol}} \\ &= (0.4 + \frac{2200}{780} \times 2.56) \times 10{-}24cm^2 \times 7.87\frac{g}{cm^3}\frac{6.022\times 10^{23}}{1g} = 0.64cm^{-1} \end{aligned} \tag{3.6}$$

The results are shown in figure 3.18. The values have been corrected for the presence of aluminium in the projection at the measured points using the aluminium attenuation coefficient determined in figure 3.14. The fit gives $0.75 \pm 0.04cm^{-1}$.

Further test will be necessary to show what physical effects lead to the deviations from the expected attenuation values. The deviations can also be due to the effects described in section 3.3.5.

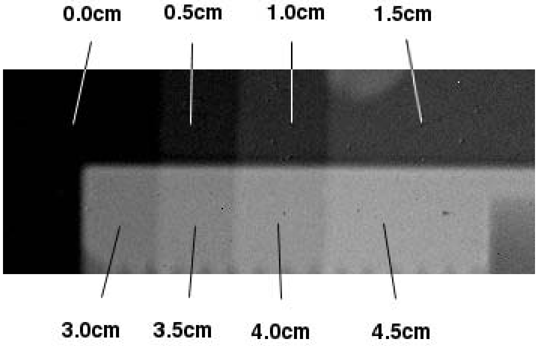

Figure 3.13: Radiography image of aluminum

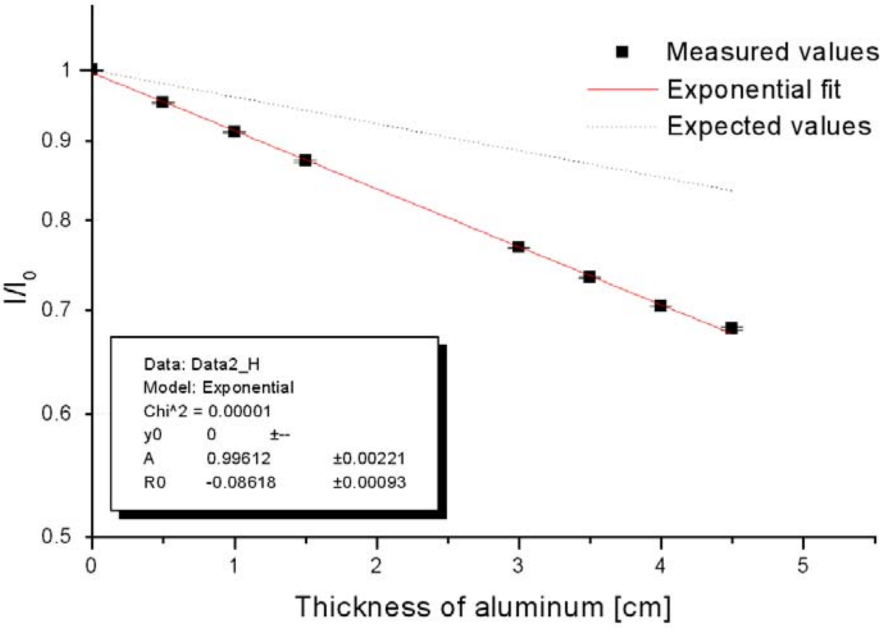

Figure 3.14: Measurement of the attenuation by aluminum. Fit function $y = y_0 + A\exp(R_0 x)$.

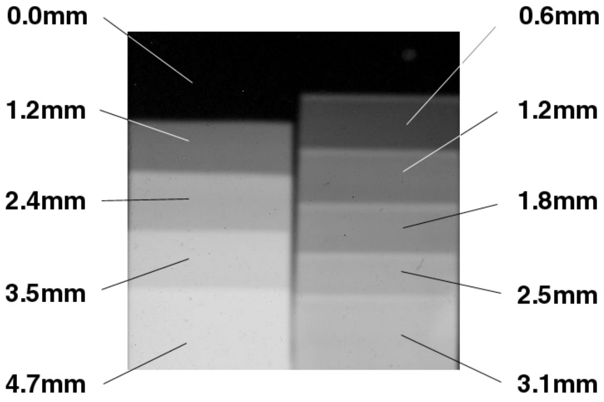

Figure 3.15: Measurement of the attenuation by acryl glass.

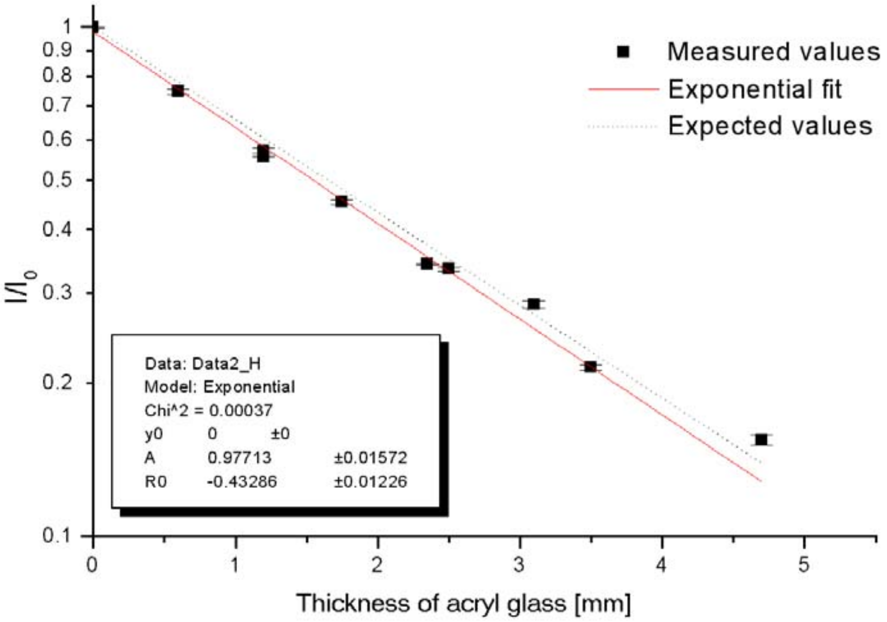

Figure 3.16: Attenuation by acryl glass. Fit function $y = y_0 + A\exp(R_0x)$.

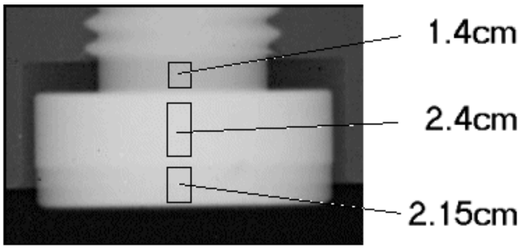

Figure 3.17: The attenuation of steal was determined from a normal projection image.

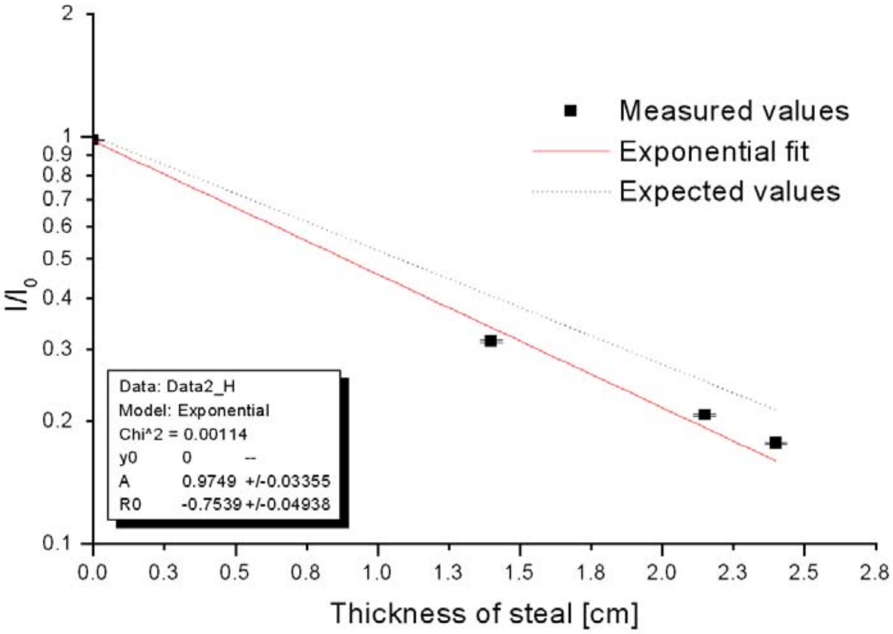

Figure 3.18: The beam attenuation by the steal screw. Fit function $y = y_0 + A\exp(R_0 x)$.

3.5 Implementation of the back projection with the Intel Performance Library for Image Processing

Using the methods of the Intel Performance Library for Image Processing (IPLib, see [Int01]) for reading and writing, convolving and rotating and performing simple mathematical operations on images, the back projection can be implemented by the following steps

- reconstruct one horizontal 2d slice from the corresponding lines of the projection images. Do this by carrying out the following steps:
  - Read a line from the projection file
  - Filter the projection line with the ShepLoagan filter (equation 2.8)
  - Create a square image with a stripe pattern according to the values of the filtered projection line.
  - Rotate the image about the angle Φ
  - Add the turned image to the current layer. This corresponds to projecting the values back to the object space.
- To reconstruct the complete object do this for every layer separately.

There are other packages commercially available that directly provide back projection algorithms. An example is IDL from Research Systems. An implementation with IDL is probably faster than this one. The implementation with the Intel Performance Library for Image Processing was used for all the reconstructions in this thesis, because the library is free and it can easily be integrated in a C/C++ program as a dynamic link library. The IPLib implementation performs the reconstruction from a set of 180 projections with dimensions 440x480 in about 2 hours on a 230MHz Pentium processor. For most of the reconstructions described in the following chapters the resolution resolution of the images was reduced to improve the processing time.

3.6 Artifacts in tomographic reconstruction

3.6.1 Insufficient number of projections

We saw in section 2.2.5 that the condition for the number of projections is

$$M \geq 2\pi r_{max}\nu_{max} \tag{3.7}$$

We will check this with the examples shown in figure 3.19. The size of the projections was 110 pixels and the reconstruction dimensions for a layer are 110 x 110 pixels. the bottom row with the reconstructions from 180 projections still show some artifacts. They are due to the effects discussed below. Here we only consider the artifacts that arise from the number of projections used for the reconstruction. The reconstruction area is a circle and the different gray values in the corners of each little picture resemble the fact, that there are no values calculated. They are thus not artifacts but the border of the reconstruction plane.
If we express πr_{max} and ν_{max} in terms of pixels we have $r_{max} = 110/2 = 55$ and $\nu_{max} = 1/2$, because the highest frequency in a line of pixels is an alternating pattern with the period 2 pixels. We get

$$M \geq 2\pi \times 55 \times 0.5 = 173 \tag{3.8}$$

Figure 3.20 demonstrates the situation in fourier space. We said, the maximum frequency in the data is 0.5. We can use the Nyquist theorem to calculate the maximum frequency that can be reconstructed from a certain number of projections.

$$\nu_{max} = M/2\pi r_{max} \tag{3.9}$$

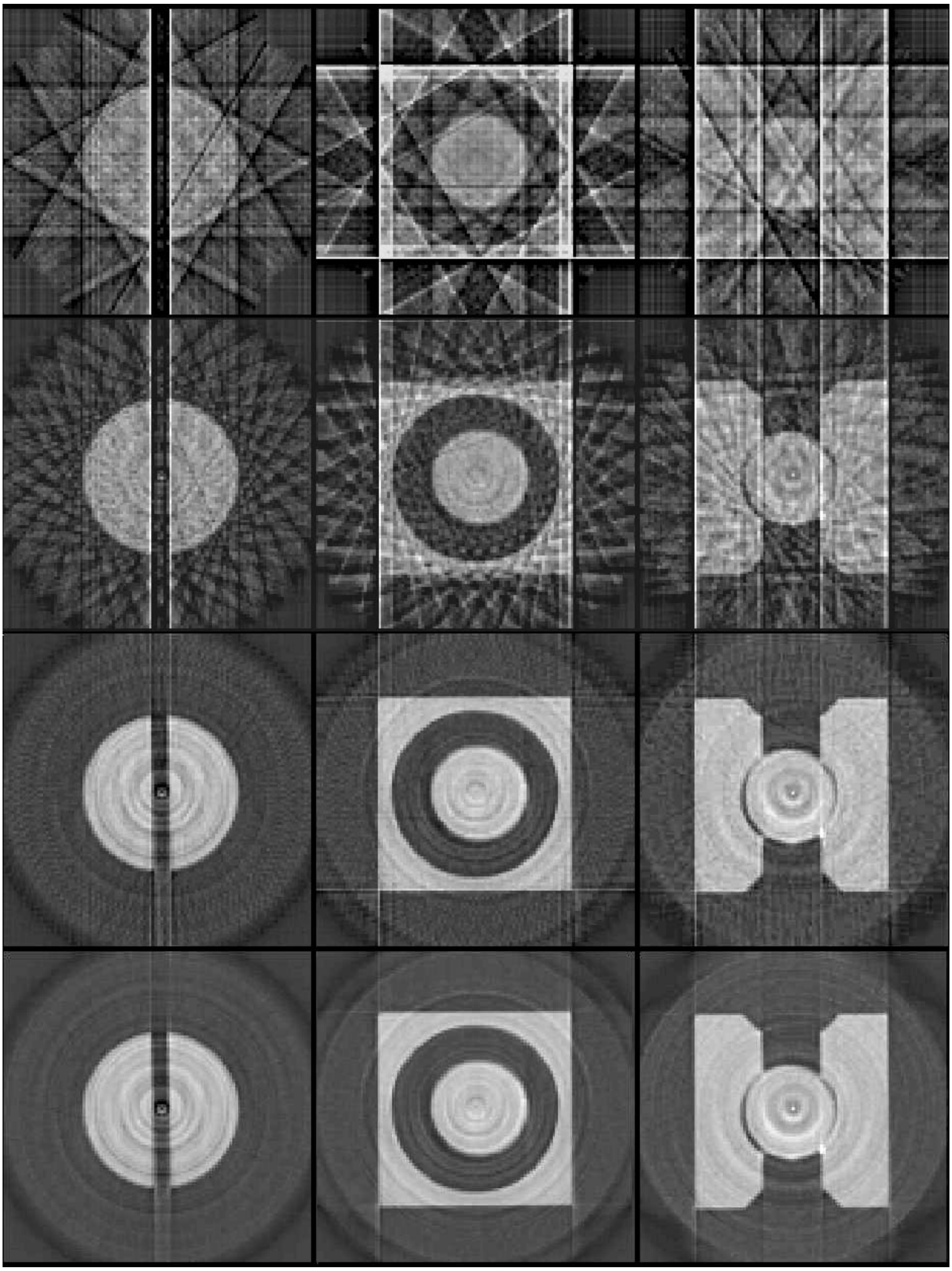

Figure 3.19: Reconstruction of three different horizontal slices of the aluminum test sample from 6, 15, 60 and 180 projections.

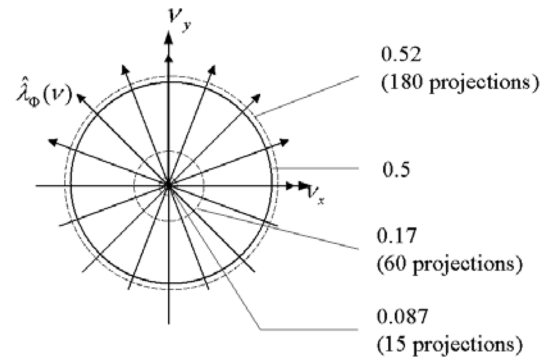

Figure 3.20: Maximum frequency for a given number of projections according to the Nyquist condition in units of pixel distance for the example with $r_{max} = 110/2$ shown in figure 3.19. Shown is also the frequency 0.5 according to the maximum representable frequency (alternating pattern).

The dashed circles indicate the maximum frequency that can be reconstructed without artifacts in this example. All the larger frequencies outside of the dashed circle are not reconstructed correctly. We can see this easily in figure 3.19. The fewer projections where used, the lower is ν_{max} and the larger structures make up the artifacts.

3.6.2 Inherent artifacts of the filtered back projection

In the reconstruction we see that the objects of strong attenuation are smeared out. In figure 3.21 the aluminum parts are disturbed by the artifacts of the stronger attenuating parts. In section I.2.3 and I.6.1 of [Sch99] is explained that these effects are due to the shift of the energy spectrum as the beam passes through the sample and to the non ideal character of the reconstruction filters introduced in section 2.2.4. Slower neutrons are attenuated stronger than the faster ones. After passing a part of the sample, the spectrum of the neutron beam has shifted to higher energies. The attenuation here is therefore different due to the energy dependence of the attenuation coefficient, i.e. the absorption cross section. The lower gray values of the weakly attenuating objects are in the same range as the artifacts of the structures with high grey values.

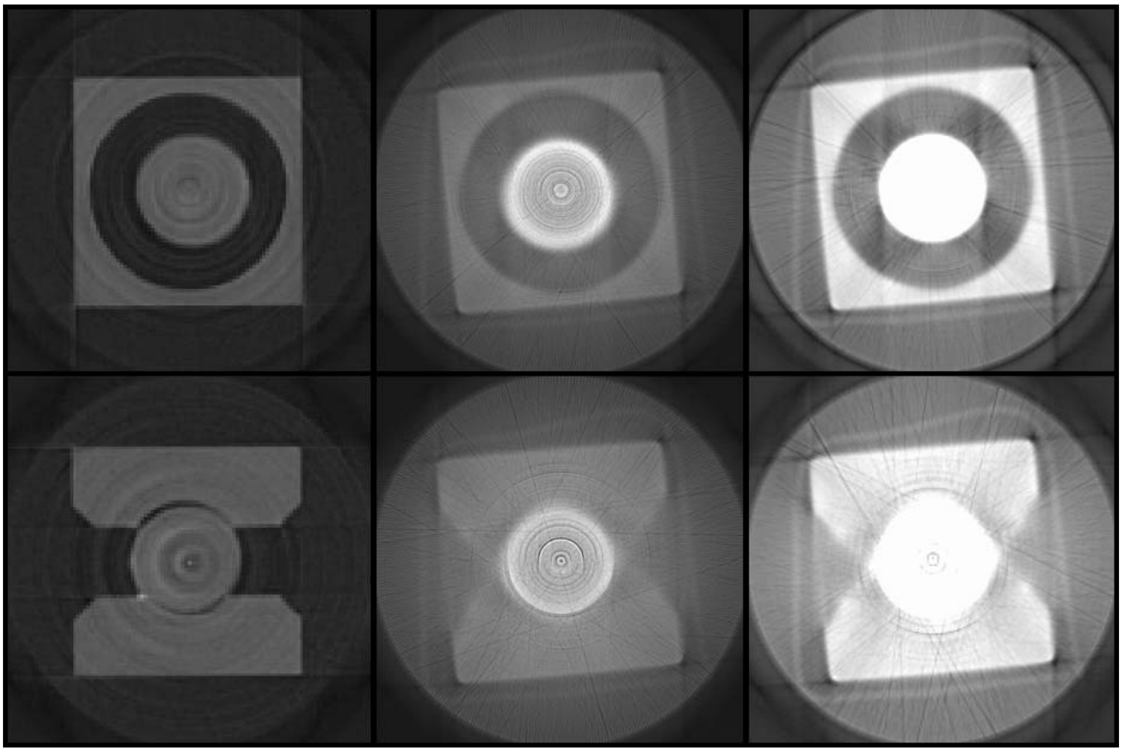

Figure 3.21: Left: Aluminum. Center: Steal screw in aluminum. Right: Plastic screw, steal case, aluminum plate.

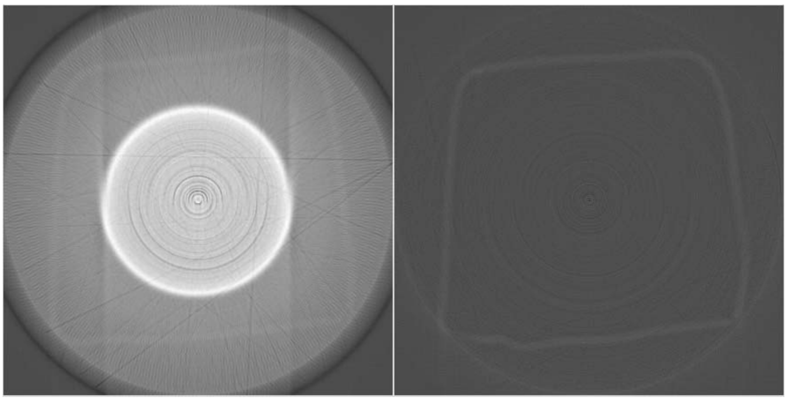

Figure 3.22: Two slices of a single reconstruction. The gray values of the background depends on the present materials. On the right, only the aluminium plate is present.

The filter used for the back projection algorithm suppresses the fourier components of the projection with ν=0. These, however, give the mean gray value of the reconstructed layer. The gray value that represents a certain attenuation coefficient thus can vary for different layers of the reconstruction set. In layers containing strongly attenuating elements the attenuation coefficients are represented by higher gray values. There should be existing solutions to this problem, which must be included in future implementations of the reconstruction. This effect can be seen very clearly in figure 3.22. The gray value of the background depends heavily on the materials in the layer. Where the steal screw is present (left), the background gray values are much higher than in the layer that contains only aluminum (right). The shown images are two layers of the same reconstruction of the steal screw, the aluminium block and the aluminium plate. In the right picture only the aluminium plate, which was wrapped around the block, is present.

3.6.3 Strong or total absorption of the beam

If the sample attenuates the beam so strong that the remaining intensity is not measurable any more, the intensity on the corresponding CCD pixel is either 0 or has a value according to the noise level. If the value is 0, it has to be corrected to the smallest value of I/I_0 that can be detected by the system. Otherwise, there are infinite values in the calculated absorption coefficient.
In such a situation the measured values do not represent the object properties any more. The lower right picture in figure 3.21 is an example, where the measured intensity is already very low due to the high attenuation by the plastic screw.

3.6.4 Wrong position of the rotary axis

A mismatch of the rotary axis causes typical artifacts in the reconstructed data. Figure 3.23 demonstrates the effect of a reconstruction with mismatched rotary axis. The dimensions of the reconstructions are 110x110 pixel according to 110 pixels per projection line. The left column shows the reconstruction with the correct rotary axes. The other two columns show the reconstruction when the rotary axis is missed by two (middle) and by four pixels (right). The distance Δx by which the rotary axis was missed is clearly visible in the reconstructions. We consider the round object in the middle of the reconstruction in the second line and the rightmost column. The radius of its lower half is larger than the one of its upper half. The difference in radius is exactly $2\Delta x$. We can see the difference most clearly at the transition from one radius to the other on the left and on the right of the object in the height of its center. The effect is also visible at the vertical edges of the rectangular objects. To express this in the terminology introduced in section 2.3.2, the point spread function of the projection and back projection with the rotary axes mismatched by Δx is a half circle with radius Δx. The vertical lines at the edges of the rectangular objects in the leftmost column indicate a remaining sub pixel inaccuracy of the rotary axis used for the reconstruction.

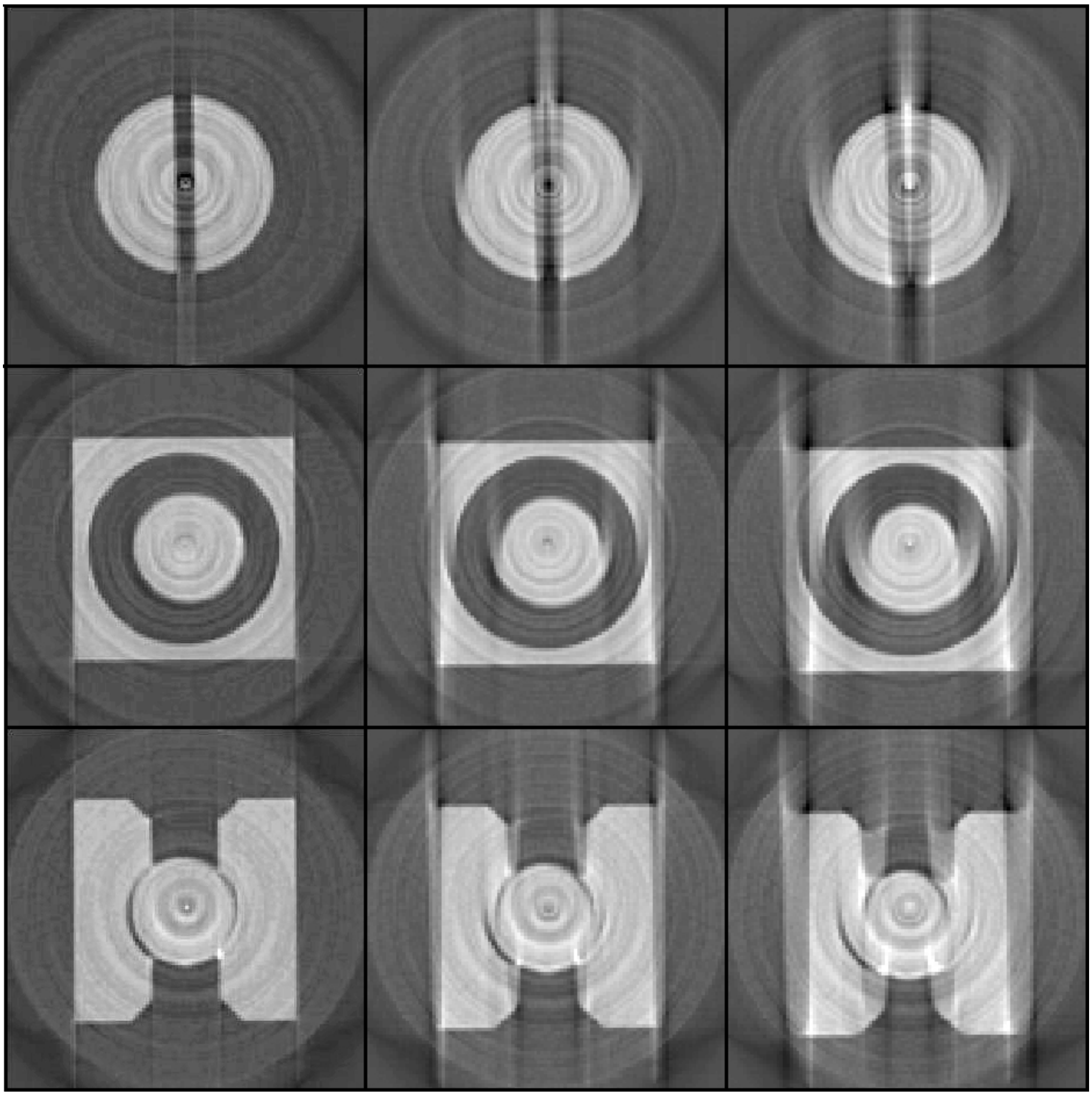

Figure 3.23: Artifacts from mismatched rotary axis. The left column shows the reconstruction with the correct rotary axis. The other two columns show the reconstruction when the rotary axis is missed by two (middle) and by four pixels (right). The projections have 110 pixels per line.

3.7 Quality of the achieved reconstruction

The test samples were reconstructed from projections with 0.3mm resolution. The resolution of the reconstructed three dimensional data was 0.4mm. This was determined from the fact that a sharp edge in the object was represented by a change of the gray values over 0.3mm in the projections and 0.4mm in the reconstructed data. With the distance of 10 cm between sample and scintillator the expected resolution was about 0.3 cm for 3mrad beam divergence. This is exactly the resolution found for the projection images. The resolution in the reconstruction is slightly reduced compared to that. Figures 3.24 and 3.25 show how the resolution was determined.
There are still a number of artifacts in the data. The reduction of the problems described in the above sections should be the goal for further implementations. Non-uniform half-circle-shaped

artifacts in the data are probably due to insufficient accuracy of the rotation axis position.

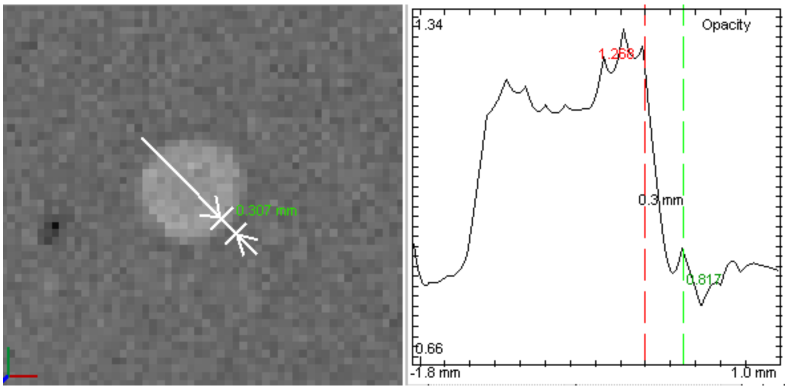

Figure 3.24: 2D resolution of the projections determined from the image of a sharp edge. The white arrows on the left indicate the distance visible between the dashed lines on the right.

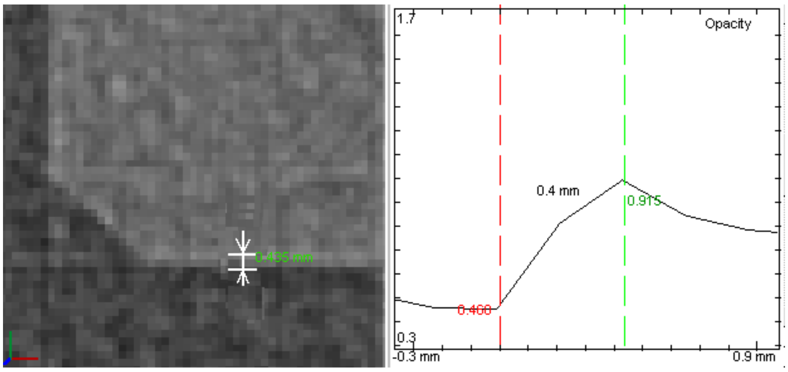

Figure 3.25: 3D resolution of the reconstructed data determined from the reconstruction of a sharp edge. The white arrows on the left indicate the distance visible between the dashed lines on the right.

3.8 Three dimensional representation and segmentation of the data

Once the reconstruction is done, the next step is to interpret the reconstructed data. In general different materials are represented by gray values according to their attenuation coefficient. For all visualization and segmentation tasks for this diploma thesis the software VGStudioMAX from Volume Graphics (see [Vol01]) was used.

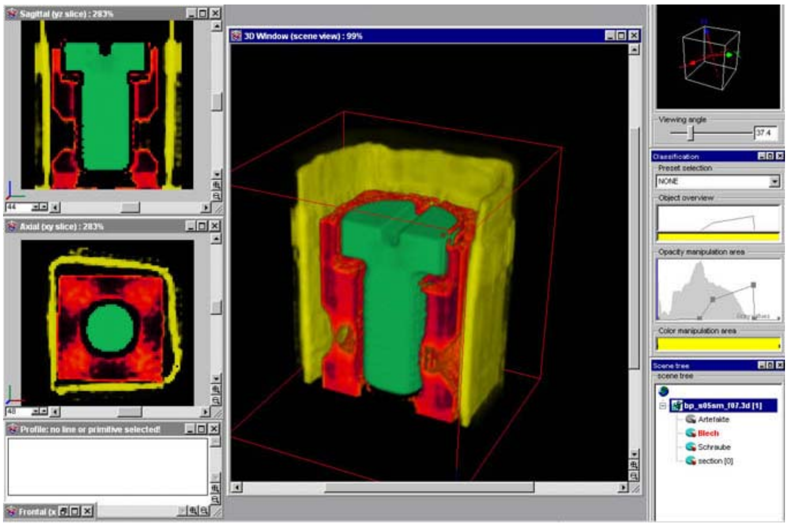

Figure 3.26: Segmentation of 3D data

Segmentation can be done in three ways.

- **Simple gray value segmentation** In the simplest case there is one object of interest in a homogeneous medium. The object can then be extracted by throwing away anything that has different gray values. This works only for simple objects with clear contrast.

- **Segmentation with a propagation method**. Start at a point and include all points that differ less than a given threshold value from the gray value at the starting point. An alternative method is to use a dynamic reference value so that all points are included whose gray values don't differ more than the threshold value from the already included values up to a certain distance. The dynamic propagation segmentation method allows segmentation of objects when the gray values of the object and the containing medium vary over the objects extension.

- **Segmentation by hand**. There are cases where the shape of the desired structure is visible but can't be extracted by the formerly described methods. This can be because of varying gray values over the extension of the object (for example due to artifacts) or because of the structure of the object itself.

Figure 3.26 shows an example where both gray value segmentation and segmentation by hand were used. The steal screw was easily segmented by grey value. The rest of the reconstruction volume contains the aluminum block and plate as well as reconstruction artifacts outside of the actual objects. The aluminum parts are disturbed by the artifacts of the stronger attenuating screw. It wasn't possible to separate them automatically, even though they are clearly visible in the gray value representation as one scrolls through the reconstructed data viewing single slices.

3.9 Spark plug, comparison with X-Ray tomography

A frequent application for X Ray tomography is the detection of defects in mechanical parts. For example, thin cracks in a spark plug can be found by X-Ray tomography. To apply neutron tomography to such a problem, the first question is about resolution. X-Ray devices are at hand for years and are well elaborated. Resolutions of $50\mu m$ are common with X-ray tomographs. With the setup for neutron tomography used here, the resolution is $400\mu m$ and therefore much lower than with available X-ray installations. It is, however, not the aim of the tomography project at the ILL to compete with existing techniques in terms of spacial resolution. Figure 3.27 shows the reconstruction of a spark plug from a set of 180 projections. The length of the spark plug is 7.5cm. The inside structure of the plug can be seen clearly. Figure 3.28 shows the reconstruction of another spark plug studied with an X-ray tomograph at Bosch in Stuttgart. Shown are two slices of the reconstructed data with differnt orientation. The visible area is close to the upper end of the spark plug where the spark is produced.

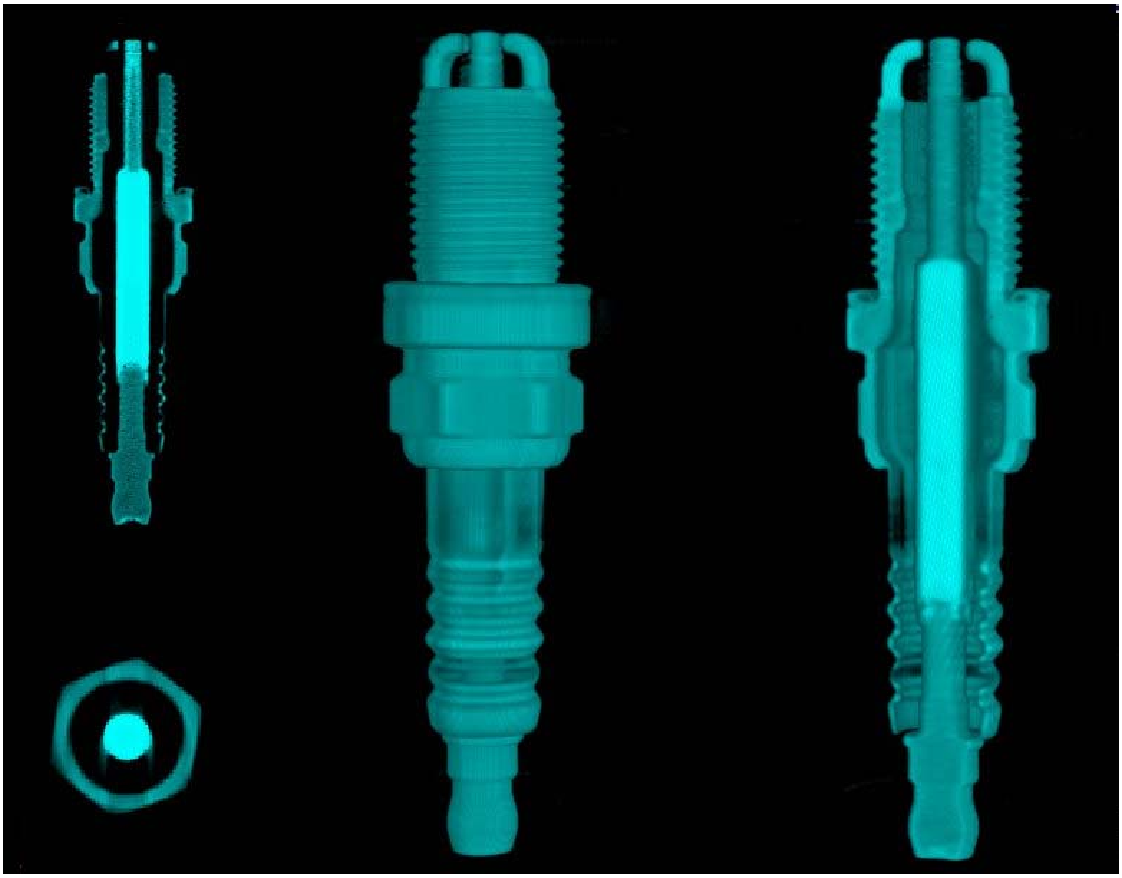

Figure 3.27: Spark plug. Reconstruction from 180 projections.

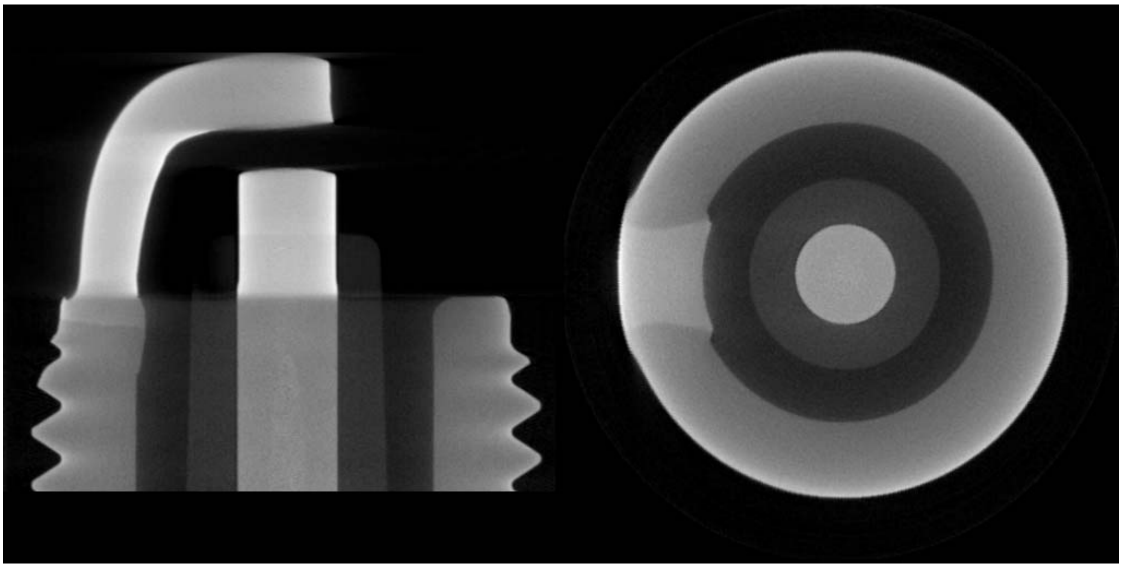

Figure 3.28: X-ray tomography of a spark plug. From H.Eisele, Bosch Stuttgart

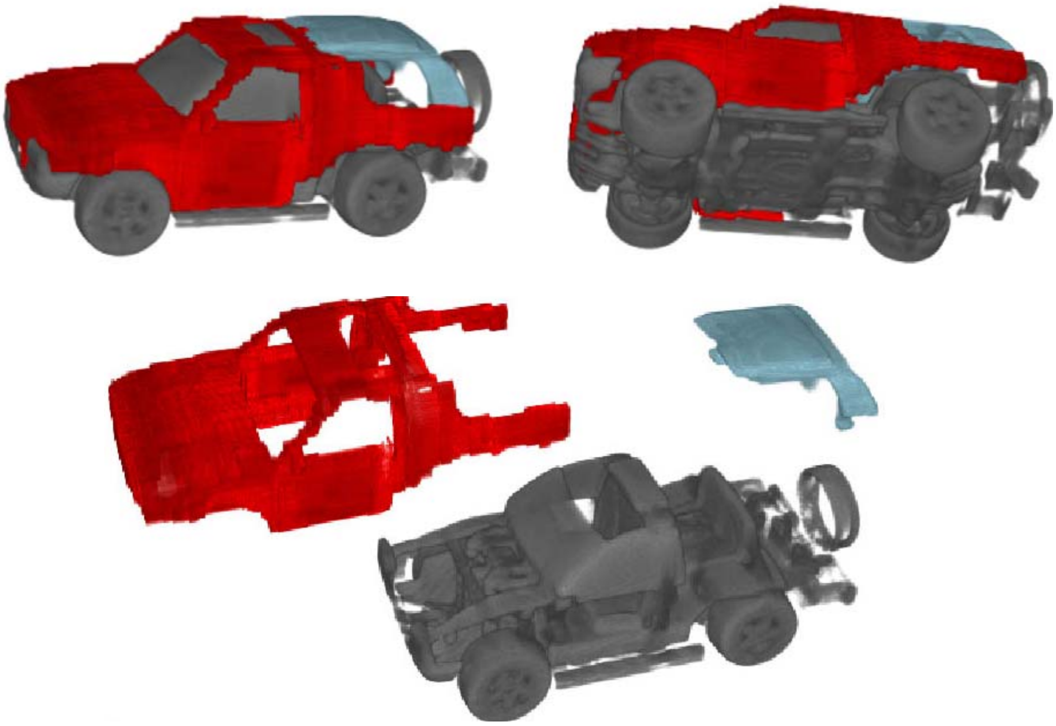

Figure 3.29: Neutron tomography of a toy car

3.10 Toy car

The tomographic reconstruction of a toy car is a nice example to demonstrate the segmentation of tomography data. All the plastic parts visible in figure 3.29 have high contrast and could therefore easily be segmented with the built in 3D segmentation tool of VGStudioMax. However the attenuation by the metal parts (red in figure 3.29) is much less and they are represented by much lower grey values. A lot of the reconstruction artifacts caused by the stronger attenuating parts lie in the same gray value range. The segmentation of the metal parts had to be performed by hand. This, however, is a time consuming task. By spending the necessary time, the quality of the segmentation of the red parts in figure 3.29 can be further improved.

3.11 Diffusion

To test the option of visualizing water distributions in stone or soil 0.8ml water were put into a plastic tube of diameter 15mm filled with sand of particle size 0.3mm to 1mm. The reconstructed data shown in figures 3.30 - 3.32 shows clearly the distribution of water which has a much higher attenuation coefficient than the sand grains.

The water was added close to the wall of the plastic tube. Therefore, the distribution is not symmetric. All parts of the data that show the plastic tube or are effected by reconstruction artifacts from the plastic tube have been cut away. The distribution of the water was static after it was added to the samd sample. The final distribution was reached within few seconds and stayed constant during the whole image acquisition process.

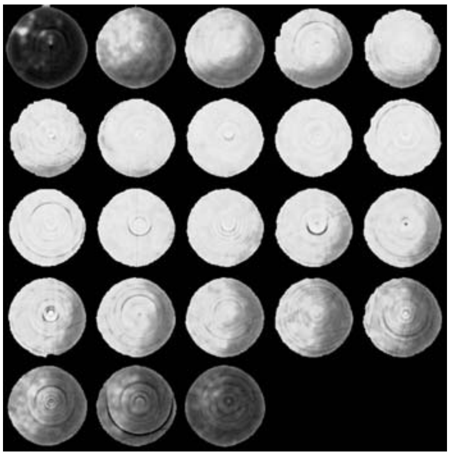

Figure 3.30: Diffusion of water in sand. Top view. Slices of the reconstructed water distribution. The top layer is the upper left image. The bottom layer is shown in the middle of the last row.

Figure 3.31: Diffusion of water in sand. Side View. Shown are vertical layers of the reconstructed distribution. Areas containing parts of the surrounding plastic tube have been cut away.

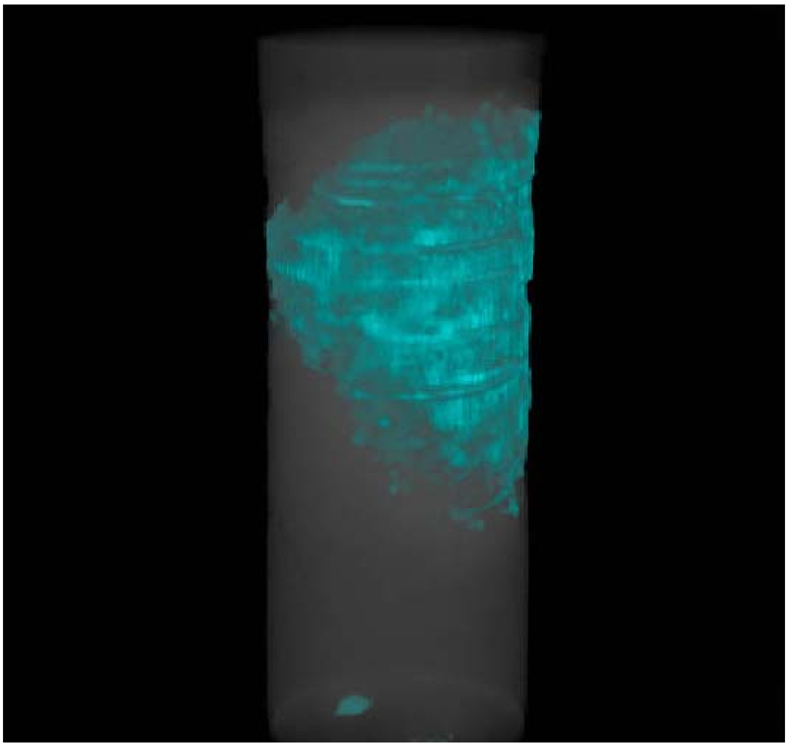

Figure 3.32: Diffusion of water in sand. Screenshot of a 3D model of the reconstructed distribution.

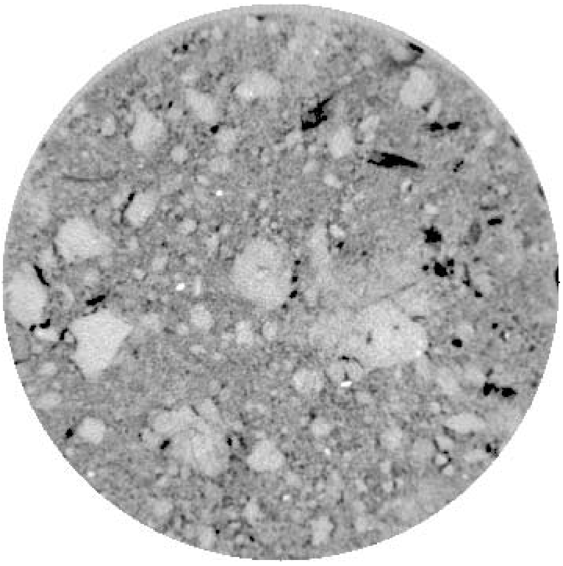

Figure 3.33: Soil sample of diameter 16cm taken with a medical X-ray tomograph. From H.J. Vogel, Institute for Environmental Physics, Heidelberg.

Further tests showed that, in general, there seems to be no strong attenuation in stones while contrast between the different components of the stones are well visible. Soil samples are also studied by X-ray tomography. An example is shown in figure 3.33 If there are water distributions in the sample, the advantage of neutron tomography is good contrast of water due to the strong beam attenuation by hydrogen. Neutron tomography of objects of this kind could support diffusion experiments like they are performed by H.J. Vogel, of the Institute for Environmental Physics in Heidelberg. Once the tomography station at the H9 beam will be operational, it will be possible to visualize the evolution of water distribution in a porous material.

Chapter 4

The tomography station at the H9 beam of the ILL

4.1 General setup of the tomography station

The ILL's high flux reactor has a performance of 58.4MW. The maximum thermal neutron flux directly at the source is $1.2 \times 10^{15} n/cm^2 s$. The tomography station is situated 15.3m away from the source behind the LOHENGRIN experiment. The expected and the measured beam intensity and divergence at this position are described in section 4.2. The LOHENGRIN experiment is a recoil mass spectrometer for unslowed fission products studying mass, kinetic energy and charge distribution of products from thermal neutron induced fission (see [Ill01]). LOHENGRIN uses only a small fraction of the neutrons available at the H9 beam. In the past all the rest of the neutron intensity was dumped in a beam stop.

A schematic drawing of the whole setup of the H9 beam with the LOHENGRIN experiment and the tomography station is shown in figure 4.14. The samples of the LOHENGRIN experiment are brought very close to the source by a movable sample holder. To avoid activation of the air by the high neutron flux, the neutrons of the beam will reach the tomography station through helium tubes with diameter 30cm. The casemate for the tomography station provides 1.6m x 2.6m room for installing the tomography setup and a lithium beam stop. Lithium doesn't produce gamma rays when it absorbs neutrons and thus avoids additional gamma intensity from the beam stop on the detector.

The inside of the tomography casemate will be covered by 1cm of boron plastic. This prevents the exposure of the casemate walls to neutrons scattered in the sample and in the detector components. To keep the inner casemate accessible a heavy concrete door separates the tomography casemate from the inner casemate.

To control the exposure of the samples and to make the tomography casemate accessible during reactor operation, the installation of a beam shutter is necessary. In the closed state, a part of the helium tubes will be replaced by a beam stop consisting of 1m heavy concrete, 10cm iron and 1.7cm B4C and Boral (BODIXAL, aluminium boron alloy). The boron absorbs thermal and slower neutrons but lets through epithermal and fast neutrons. Because the neutron scattering cross section of iron shows strong resonances in the energy range of fast neutrons, the fast neutrons are all scattered in the 10cm iron layer. The heavy concrete finally stops the remaining beam completely. The beam shutter element is mounted on a sloped rail together with a helium tube of the same length. The lower position is the closed state. To open the beam the concrete block is moved up the slope until it's completely replaced by the helium tube. In case of an eventual power failure the concrete block will move back to closed state on its own. Drawings of the shutter system and the helium tubes are shown in figure 4.2 - 4.4.

Security installations are necessary to prevent access to the casemate in case of any malfunction of the shutter that could lead to high radiation levels inside the tomography station. A locking system coupled with a detector inside the casemate will prevent access in such a case.

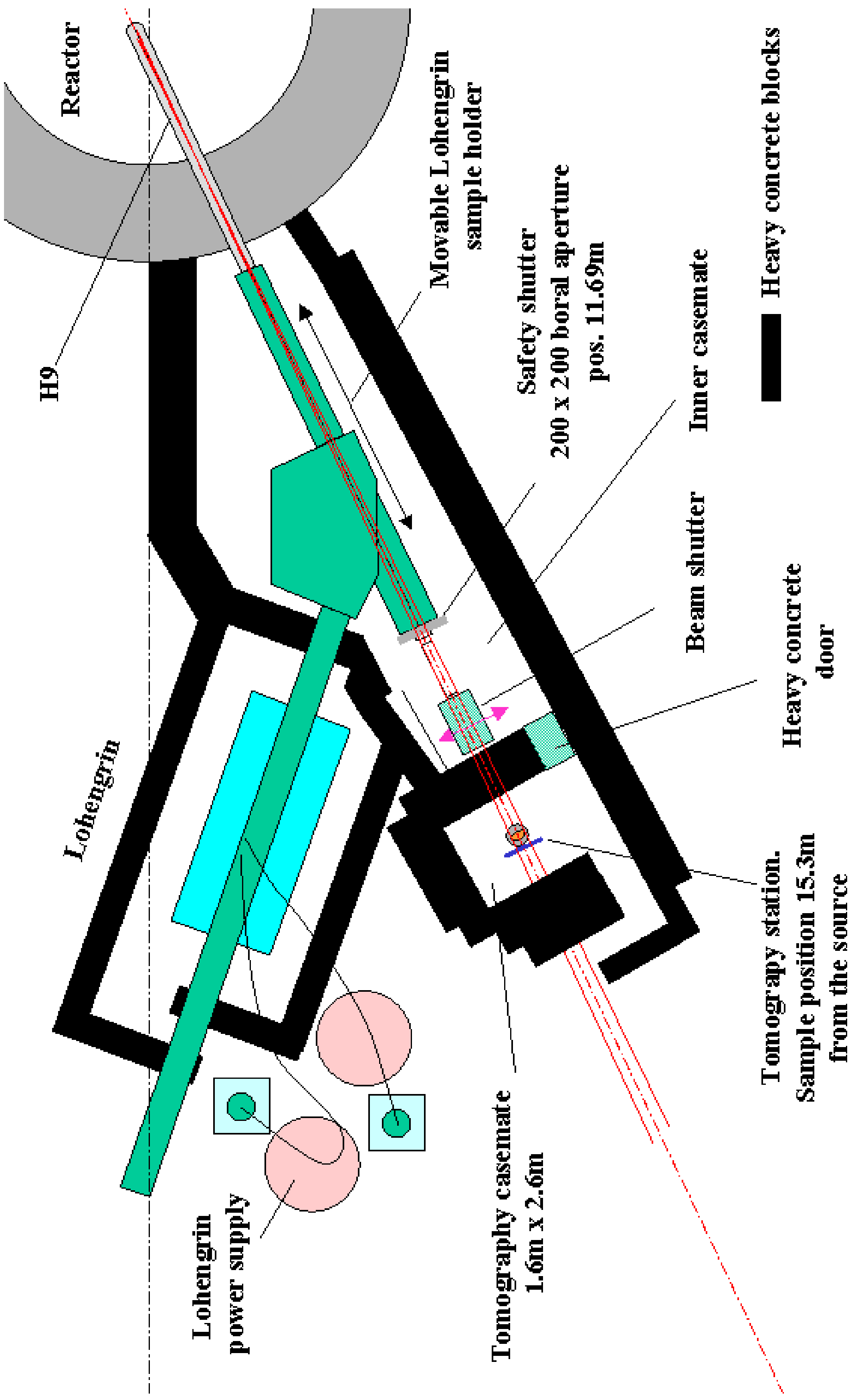

Figure 4.1: General setup of the H9 beam.

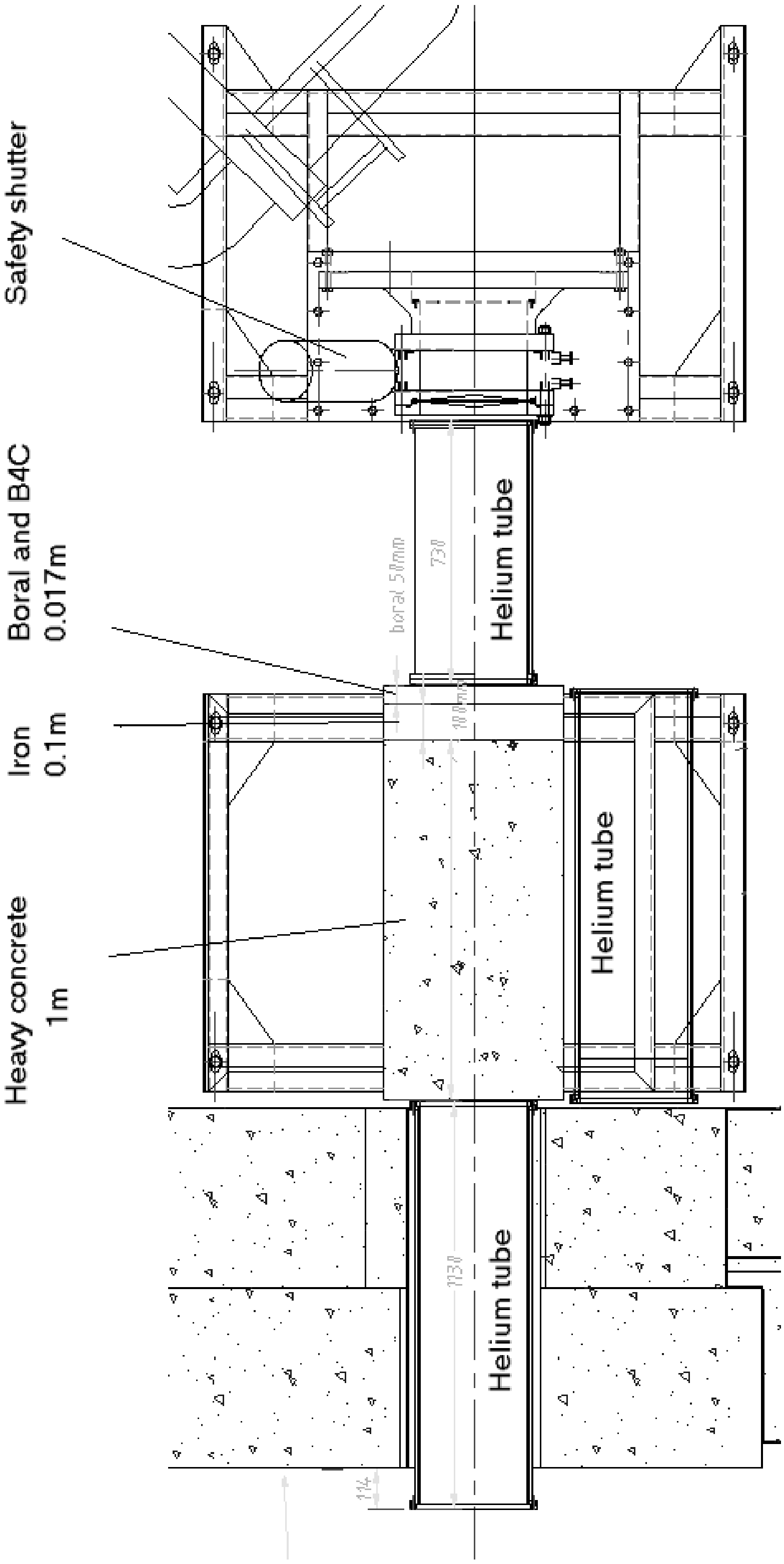

Figure 4.2: Shutter system and helium tubes. Top view. The tomography station is left of the displayed section. Drawing by ILL.

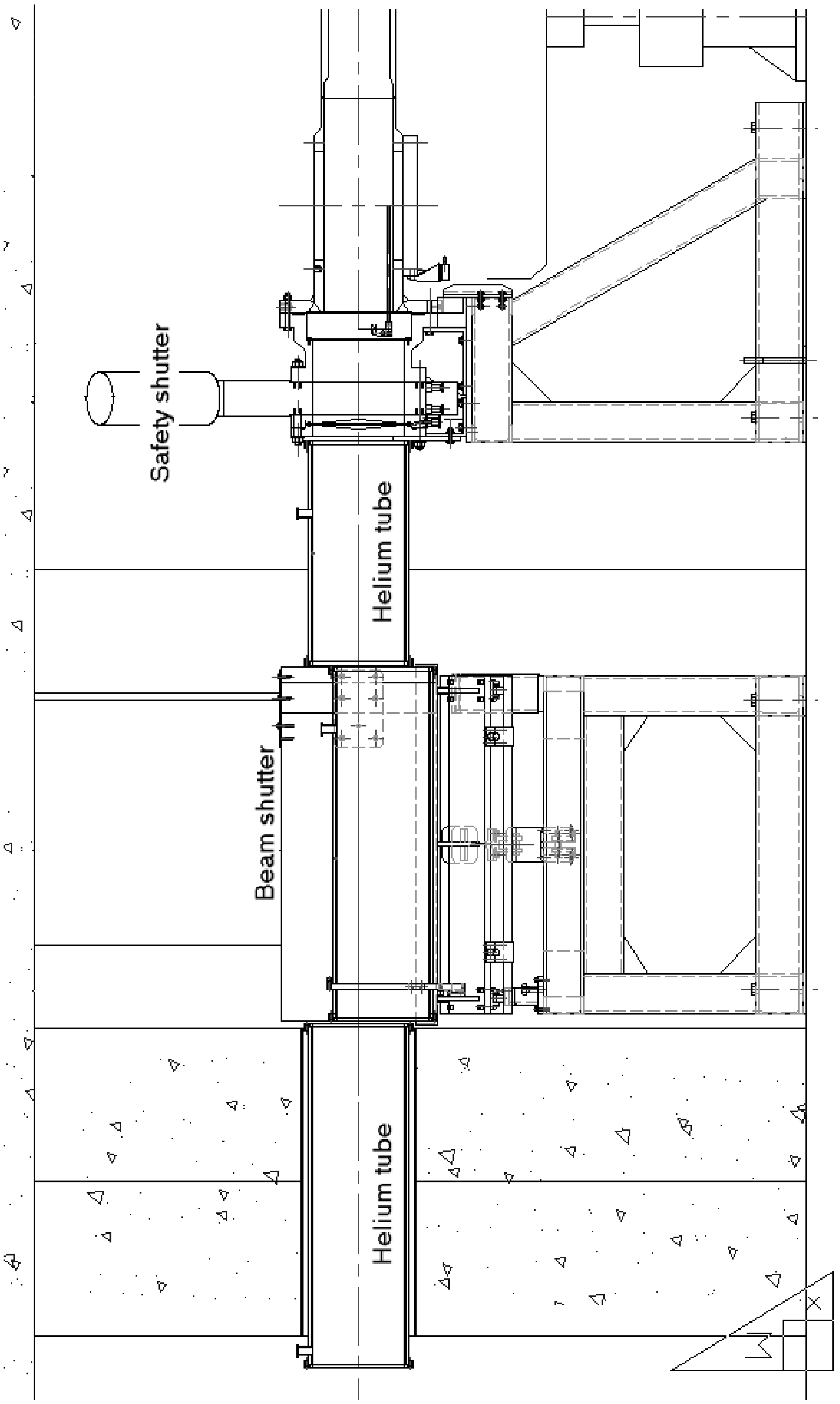

Figure 4.3: Shutter system and helium tubes. Side view. The tomography station is left of the displayed section. Drawing by ILL.

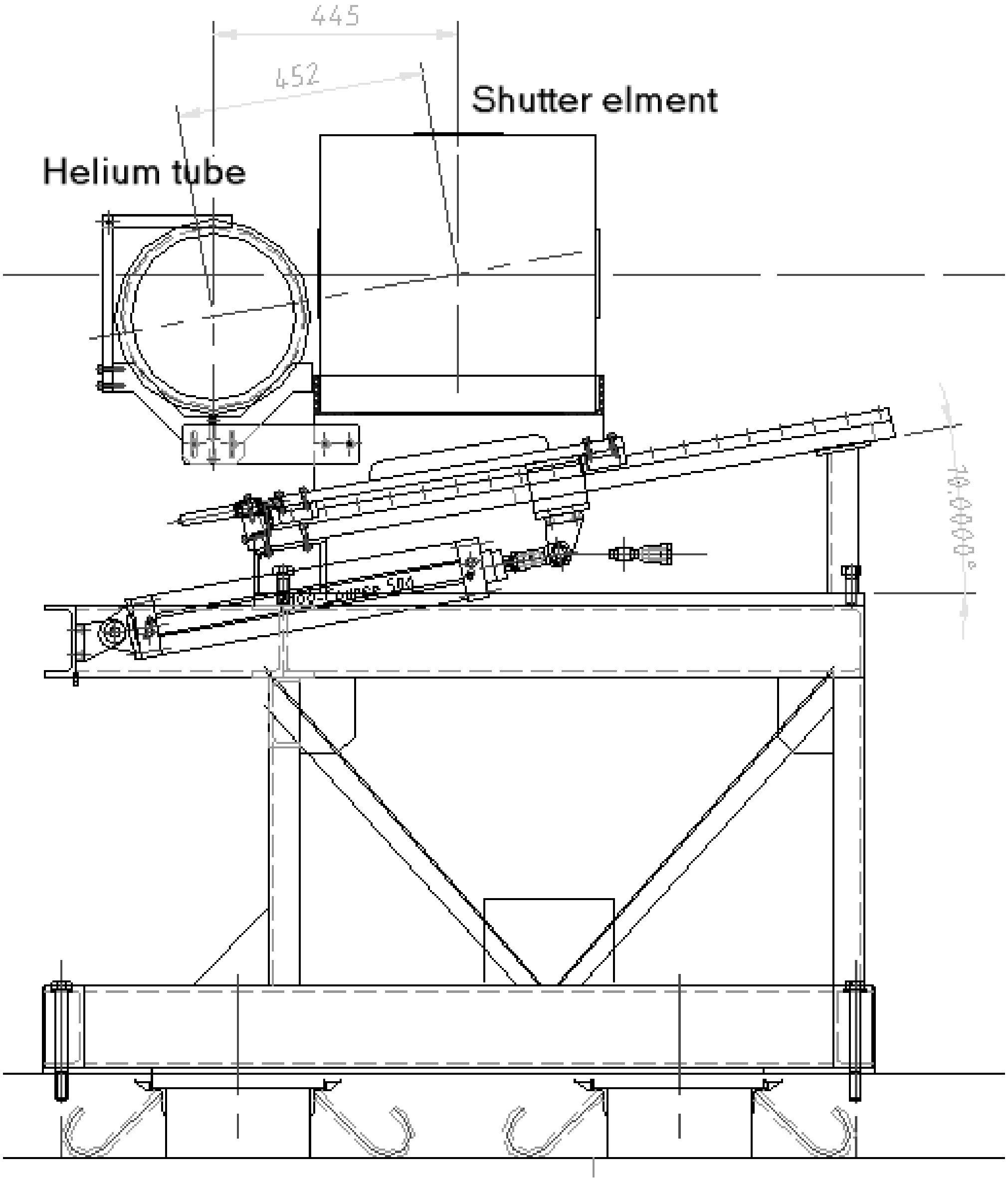

Figure 4.4: The beam shutter is mounted on a slope together with a helium tube. In open state the shutter is completely replaced by the helium tube. Drawing by ILL.

4.2 Flux and beam divergence

4.2.1 Measurement of flux and beam divergence

The measurement of flux and beam divergence of the H9 beam were performed during the first reactor cycle in 2001 when in the casemate there was no beam shutter installed yet. Only a single measurement was possible during a 20 minute test run of the reactor with nominal performance of 16.9MW compared to 58MW during normal operation. The measurements took place at the end of the current beam tube 11.7m from the source. The sample position of the tomography station will be 15.3m from the source. To get the values that hold for the tomography station the results must be corrected for these differences.

The flux was measured by gold foil activation with 16 gold foils evenly distributed over the beam cross section, together with a measurement of the beam divergence. Behind the gold foil array a Cd aperture with 16 holes of $\emptyset 5mm$ and a mutual distance of 50mm as shown in figure 4.6 was placed after the beam exit and the resulting intensity distribution in a distance of 2.52m was measured via the activation of a Cu plate (figure 4.5). The positions of the gold foils are the same as those of the holes in the Cd aperture.

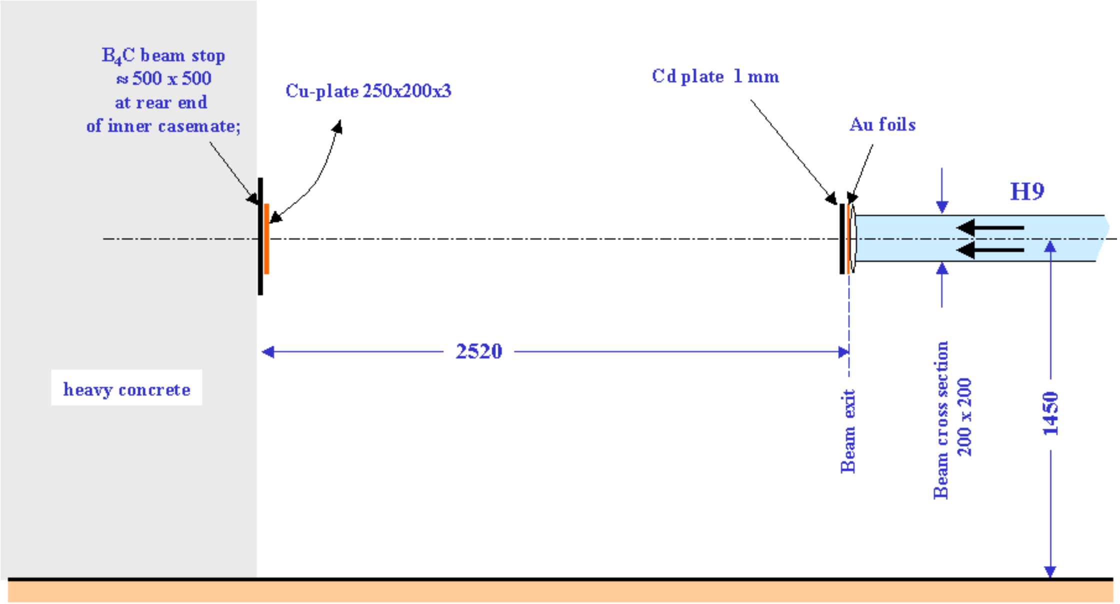

Figure 4.5: Measurement of flux and divergence of H9

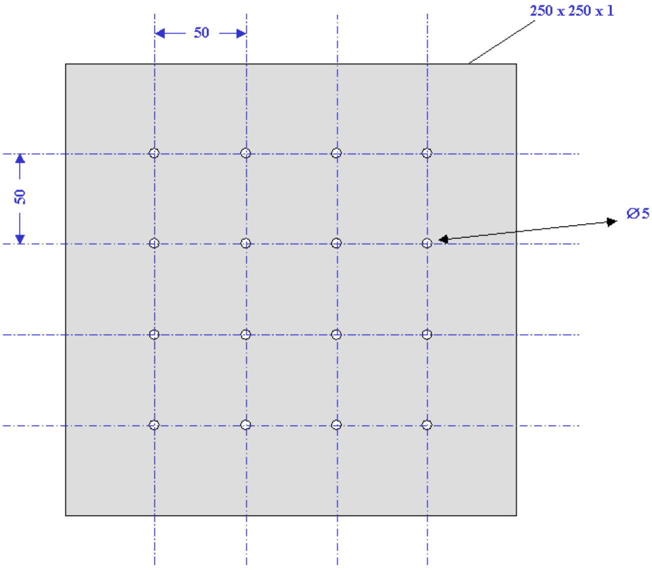

Figure 4.6: Cd aperture for measurement of beam divergence

4.2.2 Estimation of the beam divergence

The flux and divergence of the H9 beam at the position of the measurement depend on the geometrical properties of the whole setup. The source can be regarded as isotropic. Then the flux and the divergence at the measurement position are proportional to the area and diameter of the source, respectively, seen by a point in the sample.

The source is approximated by a rectangular area. The horizontal and vertical divergence are considered independent. That is, horizontal divergence depends only on the horizontal position and the vertical divergence only on the vertical position. The divergence depends on the height or width respectively seen from the sample point. The estimated values for the beam divergence in rad for the position of the measurement are shown on the right in the figures 4.7 and 4.8. All distances are given in mm. For the calculation of the vertical divergence several obstacles along the beam have to be taken into account. They are shown in figure 4.7. The expected horizontal divergence is 15 mrad at the center of the beam height independent of the horizontal position. The vertical divergence varies over the beam height due to the geometric factors indicated in figure 4.7.

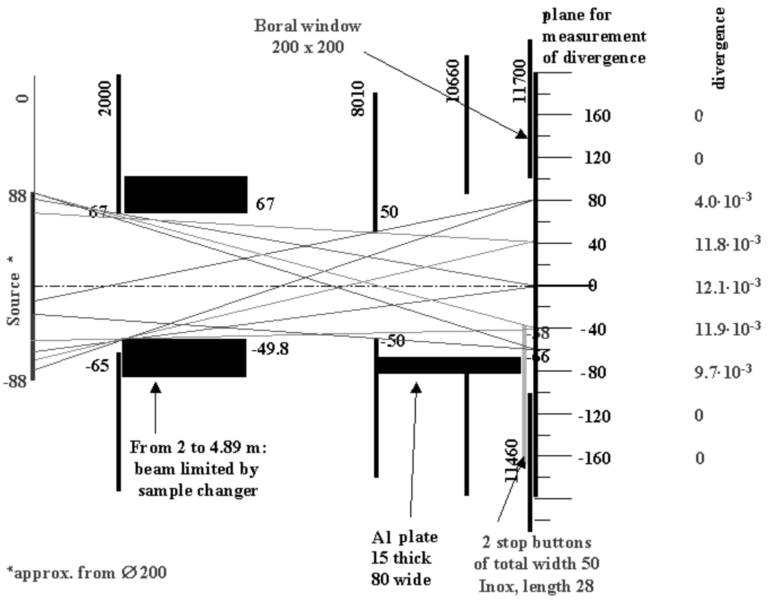

Figure 4.7: Calculated vertical divergence

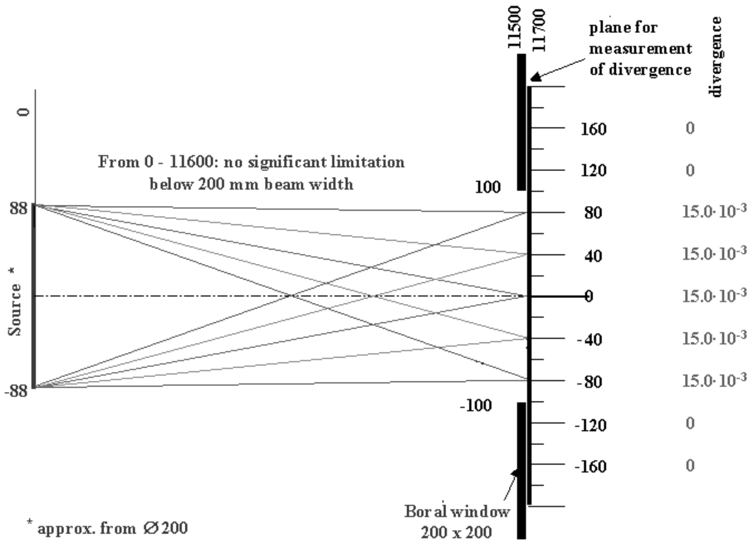

Figure 4.8: Calculated horizontal divergence

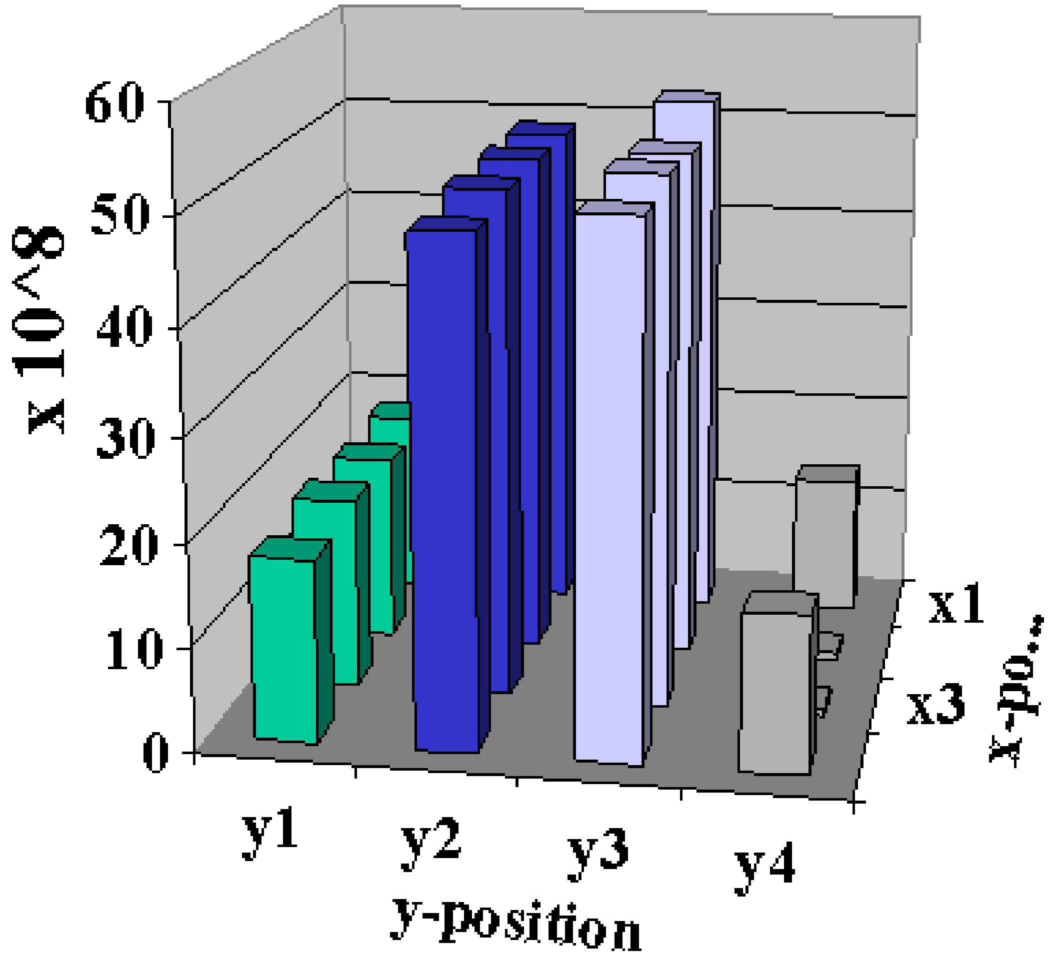

Figure 4.9: Thermal neutron flux at the position of the measurement in n/cm^2s. y1 is the position of the topmost row of gold foils, y4 the position of the lowermost row.

4.2.3 Results of the measurements

Neutron flux

Figure 4.9 shows the measured neutron flux in n/cm^2s. The values were determined by the department for radiation protection of the ILL by comparison of the activity of the gold foils with similar measurements at other beam lines. At the sample position the intensity is reduced by a factor $(15.3m/11.7m)^2 = 1.72$ compared to the values displayed. Thus, the maximum beam intensity at the sample position for the tomography station will be $2.9 * 10^9 \frac{n}{cm^2 s}$. In the middle of the lowermost row of gold foils the intensity is heavily reduced. This must be due to an obstacle in the beam close to the beam exit.

Beam divergence

The activation of the Cu plate was determined by putting it on an image plate. The result is shown in figure 4.10. Though the distance between the outer holes in the Cd aperture was 15cm (see figure 4.6), the resulting intensity pattern in 2.52m distance didn't fit on the 20cm × 25cm Cu plate. Two rows are almost completely lost because of the beam deviation. The spots are

outside of the Cu plate. The beam deviation was calculated by comparing the pattern on the Cu plate with the position of the holes in the Cd aperture. The position of the outer spots was estimated by assuming them to have the same shape as the clearly visible ones. Figure 4.13 shows the resulting beam deviation in rad depending on the off-axial position.
The spots on the Cu plate show an internal structure that varies with the position. The lower one of the two clearly visible rows of spots in figure 4.10 shows notable additional structures on the lower side of every spot. These can be due to the actual shape of the LOHENGRIN sample holder. If the reason for these structures lies close to the source, they could be produced by holes in the upper part of the sample holder (pinhole camera priniciple). In the upper rows they would then possibly be hidden due to other beam limitations also indicated in figure 4.7.
The beam divergence was determined by measuring the sizes of the spots as shown in figure 4.11. The results of the divergence measurement together with the calculated values (figures 4.7 and 4.8) are shown in figure 4.12.

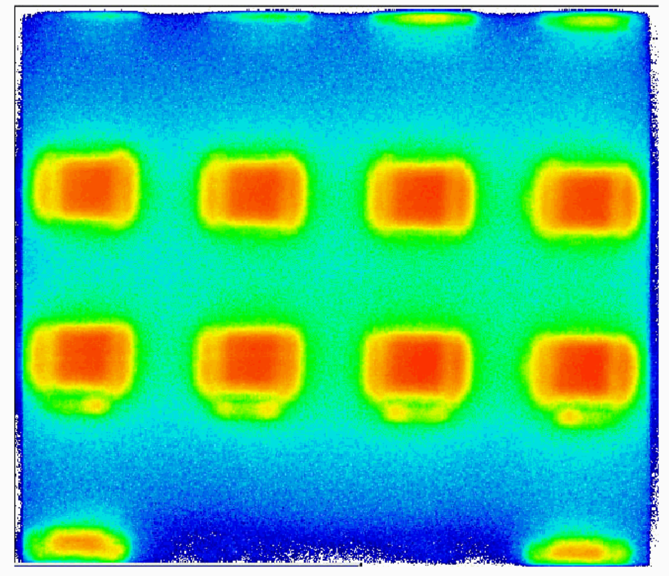

Figure 4.10: Colorized thermal neutron intensity pattern on the Cu plate, showing a non-homogeneous behavior of the beam divergence.

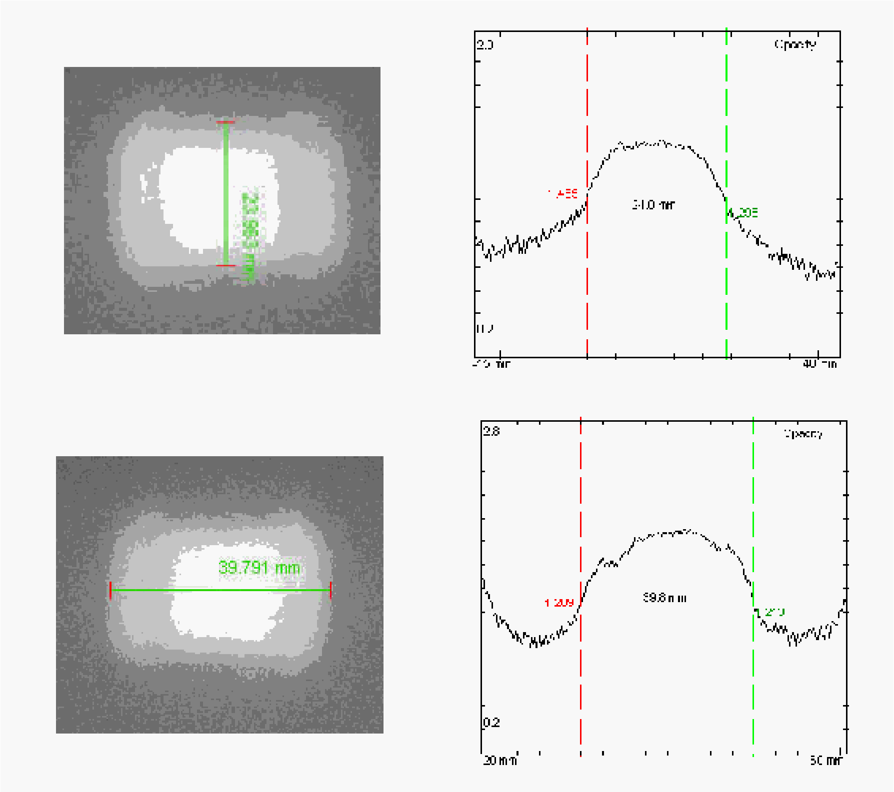

Figure 4.11: Shape of a single spot. The beam divergence was determined by measuring the sizes of the spots.

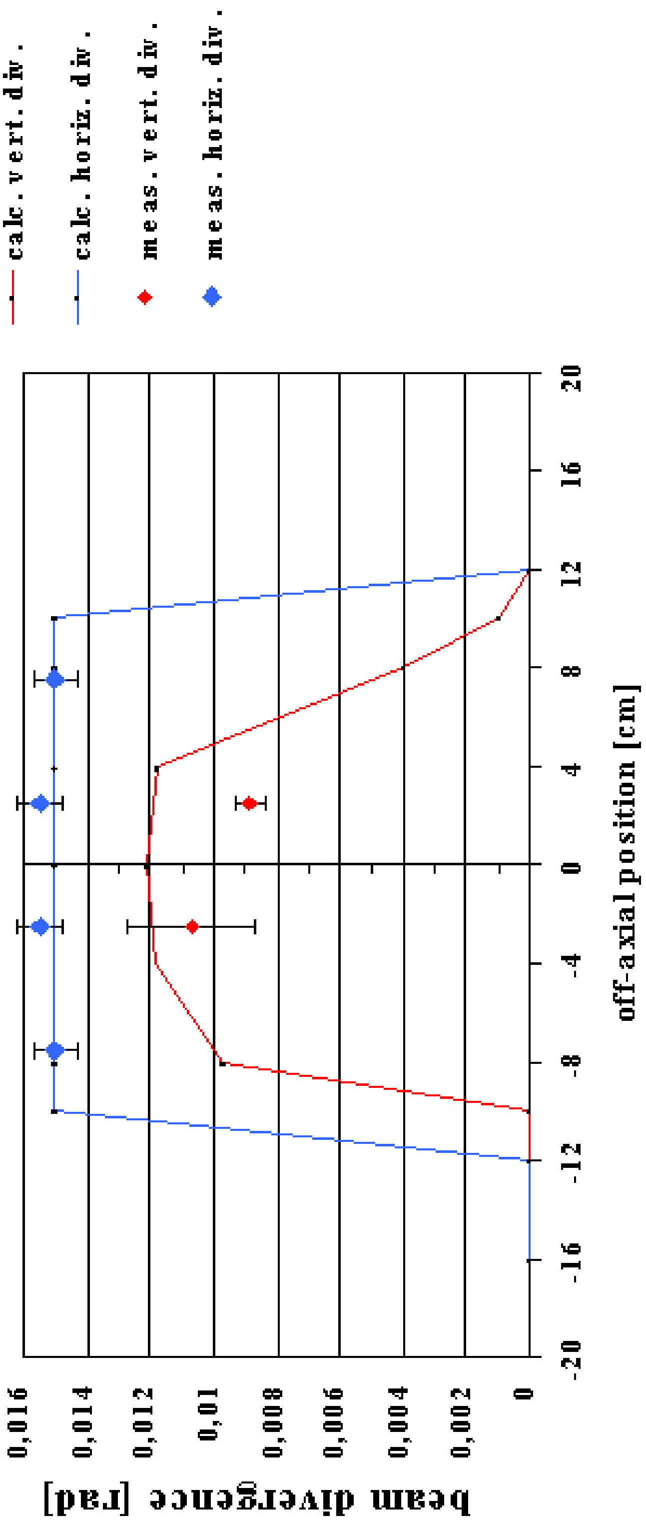

Figure 4.12: Calculated (line) and measured (points) beam divergence at the beam exit in rad.

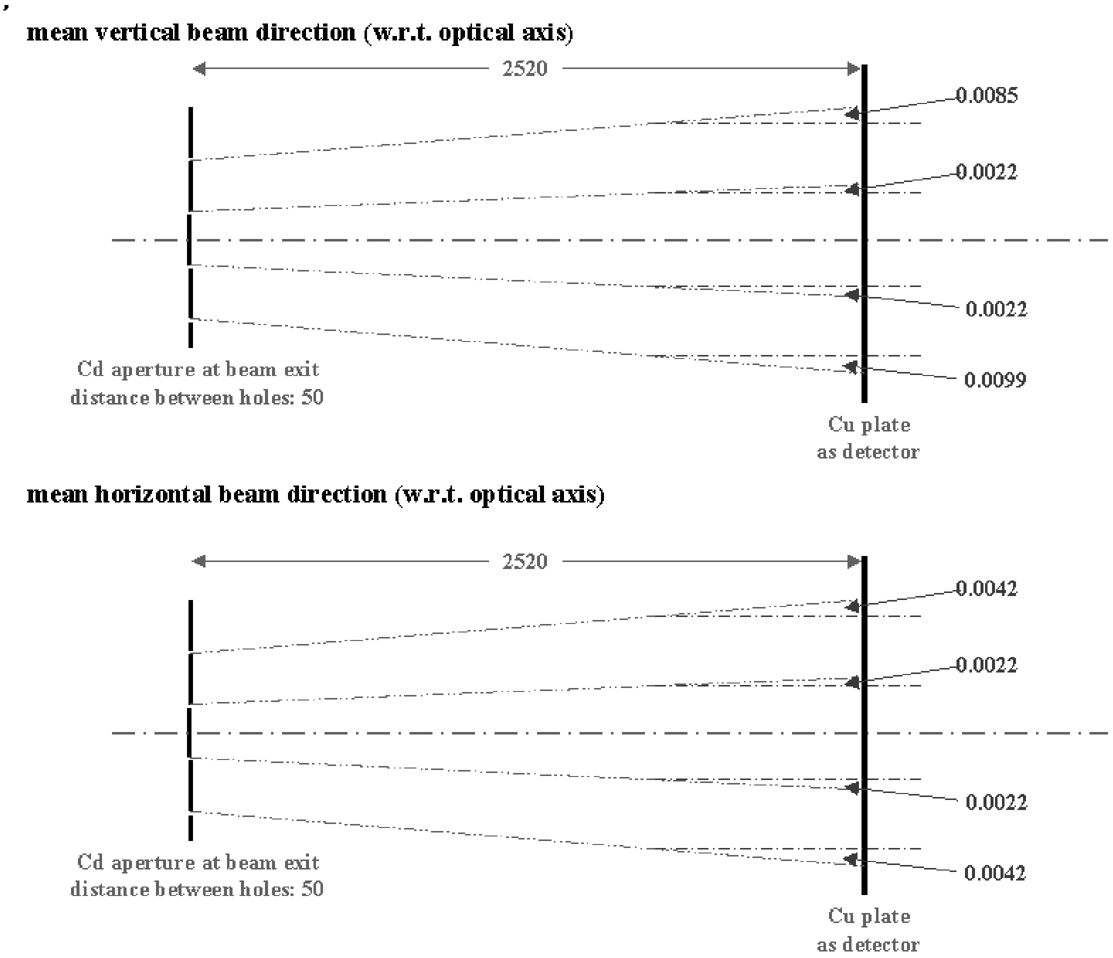

Figure 4.13: Deviation of the beam direction depending on the off-axial position of the holes in the Cd aperture.

4.2.4 Implications for the expected resolution

All the measurements were performed at a position 11.7m from the source. To get the divergence at the sample position of the tomography station 15.3m from the source the values have to be corrected by a factor 11.7/15.3 = 0.76. The measured horizontal beam divergence of 15mrad and vertical beam divergence of around 10mrad (compare figure 4.12) correspond to 11.4 and 7.6mrad at the sample position of the tomography station. This means an L/D ratio of 115 (horizontal) and 132 (vertical). The resolution for a detector in 10 cm distance of the sample is then 1.14mm in horizontal direction and 0.76mm in vertical direction.

The consequences of the behavior of the divergence for image processing will have to be discussed. The different patterns indicate a position dependent point spread function. The size of the effect on the produced images must be determined. Correction for a varying point spread function might require a lot of computing power. The Cu plate proved to be to small, so not all of the patterns are completely visible. Further measurements will be necessary, when the tomography station is ready. The beam deviation requires geometric correction of the taken images before they can be used for reconstruction.

4.3 Scintillator, Camera and optical system

General setup
The camera and scintillator must be in a closed box. The design of the box depends on the following special conditions at the H9 beam. The scintillator should be as close as possible to the sample to keep the effects of the beam divergence small. The rotary stage could be mounted on a linear stage to move it towards or away from the scintillator depending on the sample size. Because of the high flux of the H9 beam, the camera must be surrounded by sufficient shielding against

gamma rays and scattered neutrons from the sample
gamma rays and scattered neutrons from the mirror
gamma rays and scattered neutrons from the back wall of the scintillator case
scattered neutrons from the scintillator
gamma rays from the beam stop (avoidable by the use of a lithium beam stop)

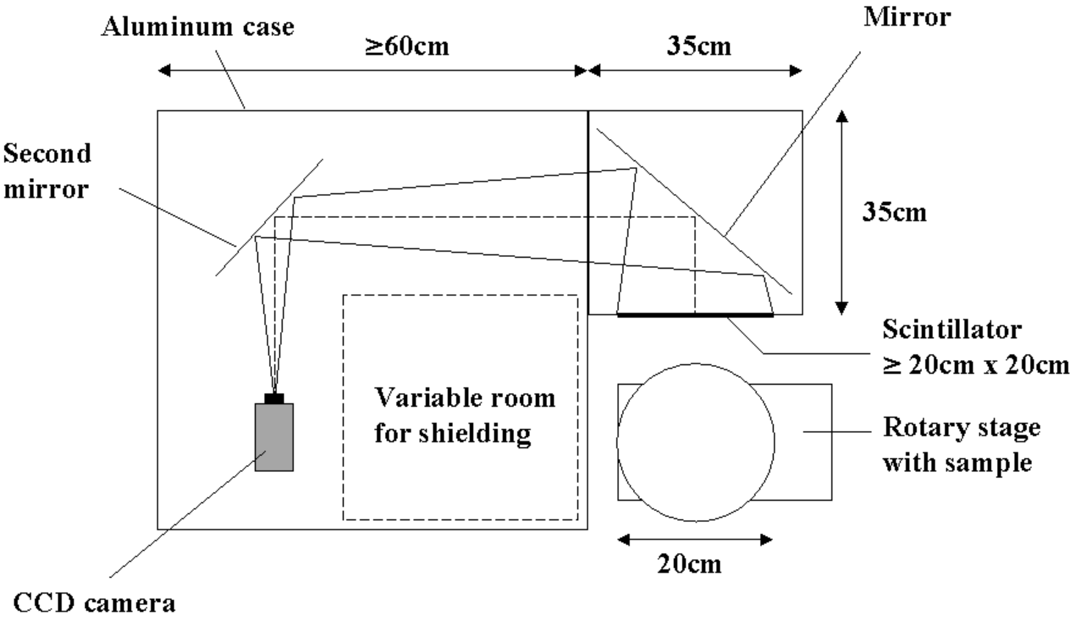

Figure 4.14: Setup for camera, scintillator and sample.

A scintillator from Applied Scintillator Technologies (NGd, ^{6}LiF:ZnS:Cu,Al,Au) with low gamma sensitivity will be used. It is based on the detection of neutrons by the reaction

$$n +^6 Li \rightarrow He +^3 H + 4.8MeV \tag{4.1}$$

Up to now, no exact specification on the light output per detected neutron could be gained from the producer. The spectrum of the emitted photons has its maximum at $\lambda = 540nm$ which corresponds to a photon energy of 2.30eV. For this estimation we assume all the photons to have this energy. 4.8MeV correspond to 2.1×10^6 green photons. We assume that around 10^5 green photons are actually emitted perpendicular to the scintillator surface per detected neutron. The detection probability for the neutrons on the scintillator is supposed to be $P_{n,sc} = 20\%$.

The scintillator size should be at least 20cm×20cm. Due to the required space for shielding, the optical distance between the scintillator and the camera will be around 1m. According to the expected resolutions of down to 0.76mm, the array size of the CCD chip should be at least 2 × 200mm/0.76mm = 526 to fulfill the Nyquist condition. If the array size is smaller, the visible size of the scintillator can be reduced by reducing slightly the camera-scintillator distance.

Effect of the chip size
We consider equation 2.41, especially the version that uses the full well capacity. As already stated in section 2.4, the full well capacity depends almost linearly on the chip size. We approximate it for a short consideration by the squared size of one chip dimension B and a constant factor β. The chip size influences also the solid angle of the chip (via the focal length). The count rate is then proportional to the term

$$\frac{1}{(f/\#)^2}\left[\left(1+\frac{G}{B}\right)^2 \beta B^2\right]^{-1} \tag{4.2}$$

The choice of the chip size determines the focal length, but doesn't influence notably the exposure time as long as the objectives have the same f/#. The f/# itself is far more important for the exposure time.

However, for a camera with a small chip and thus a very low conversion factor (conversion factor = full well / DAC range), statistical errors of the counted electrons $\Delta e = \sqrt{e}$ become important for low count rates. This reduces the effective dynamic range.

Exposure time
It is very important for a short exposure time to use an objective with an f/# as little as possible (large maximum aperture). It should be possible to find an objective with f/# = 1.0. For example, using the 12 bit camera SensiCam from PCO with 2×2 binning (1280 × 1024 → 640 × 512) and high gain (gain = 2) we have

$I_{n,0} = 2.9 \times 10^9 \frac{n}{cm^2 s}$
$G_y = 20$cm
$G_x = \frac{0.86}{0.69} \times 20$cm $= 24.9$cm
g = 1m
$P_{n,sc} = 0.2$
$\frac{dN_{ph,sc}}{dn} = 10^5$
f/# = 1.0
$B_x = 0.86$cm
$B_y = 0.69$cm
$M_x = 1280$
$M_y = 1024$
$QE_{ca} = 40\%$
fill factor = 100% (lens on chip)
conversion factor = 5e$^-$/count
DAC range = 4096 (12bit)
binning = 2×2 = 4
gain = 2

Setting these values in equation 2.41 and 2.27, this yields an exposure time of 4.2ms using the cameras full dynamic range.

Chapter 5

Outlook

The tomography station of the ILL is going to be ready in October 2001. The design favors short exposure times rather than high spatial resolution. Given the performance of the the ILLs high flux reactor, the tomography station can become an unchallenged tool in the short exposure time domain of neutron radiography and neutron tomography.

A fair amount of experience is now at hand. The preparative measurements yielded useful information on experimental details and already some very nice pictures from tomographic reconstructions. It could show the basic problems that arise during the image acquisition and reconstruction process.

Even during the test measurements the value of neutron radiography and tomography for a variety of applications became visible.

The criteria collected in section 2.3.1 and 2.4 will be used to determine the best suited camera system for the application.

The reconstruction algorithm will be implemented on a multiprocessor computer hardware system already used for fast processing of huge amounts of data from ILL instruments allowing fast reconstruction or even online representation of changes within a sample.

Bibliography

[Aud01] "The AUDINE Project",
http://www.astrosurf.com/audine/English/index0.htm

[Au201] "TWO OR THREE WORDS ABOUT CCD",
http://www.astrosurf.com/audine/English/intro/intro7.htm

[Au301] "All the details about KAF-0400",
http://www.astrosurf.com/audine/English/intro/intro5.htm

[Bil01] J.Bille, W.Schlegel: "Medizinische Physik II", Springer Verlag, 2001, ISBN 354065254X

[Ill01] "The ILL Yellow Book",
http://www.ill.fr/pages/science/IGroups/yb.pdf,
Section Instrument List, Subsection Nuclear and Particle Physics Groups.

[Int01] "Intel Performance Libraries",
http://developer.intel.com/software/products/perflib/

[Jae97] B. Jaehne: "Digitale Bildverarbeitung", Springer Verlag, 1997, ISBN 3-540-61379-X

[Leh99] "Neutron Tomography",
http://asq.web.psi.ch/ASQ/projects/Neutron_Tomography.html

[Mun00] D. Mund: "Aufbau eines Experiments zur Messung der Neutrinoasymmetrie im Zerfall freier Neutronen", Diplomarbeit, Physik, Universitaet Heidelberg, 2000.

[Nas01] "FITS Support Office Home Page",
http://fits.gsfc.nasa.gov

[Rad17] J. Radon: "Ueber die Bestimmung von Funktionen durch ihre Integralwerte laengs gewisser Mannigfaltigkeiten.", Ber. Verh. Schsische Akad. Wiss., Leipzig, Math. Phys. Kl 1917:69,S262-277

[Rei01] H. Reitmayer: "Lichtgroessen",
http://www.reitmayer.de/phligroe.html

[Rop01] Roper Scientific,
http://www.roperscientific.de

[Sch99] B. Schillinger: "Neue Entwicklungen zu Radiographie und Tomographie mit thermischen Neutronen und zu deren routinemaessigem Einsatz", Dissertation Technische Universitaet Muenchen, 1999

[Vol01] Volume Graphics,
http://www.volumegraphics.com/

I declare that I wrote this thesis independently and that I didn't use any other sources than the ones indicated.
Heidelberg, 07/01/01